

## Microwave-Assisted Spectroscopy Technique for Studying Charge State in Nitrogen-Vacancy Ensembles in Diamond

D.P.L. Aude Craik<sup>1,\*</sup>, P. Kehayias<sup>1,2,‡</sup>, A.S. Greenspon<sup>3</sup>, X. Zhang<sup>3,§</sup>, M.J. Turner<sup>1,4</sup>, J.M. Schloss<sup>4,5,§</sup>, E. Bauch<sup>1</sup>, C.A. Hart<sup>1</sup>, E.L. Hu<sup>3</sup>, and R.L. Walsworth<sup>1,2,4,6,7,8</sup>

<sup>1</sup>Department of Physics, Harvard University, Cambridge, Massachusetts, USA

<sup>2</sup>Harvard-Smithsonian Center for Astrophysics, Cambridge, Massachusetts, USA

<sup>3</sup>John A. Paulson School of Engineering and Applied Sciences, Harvard University, Cambridge, Massachusetts 02138, USA

<sup>4</sup>Center for Brain Science, Harvard University, Cambridge, Massachusetts 02138, USA

<sup>5</sup>Department of Physics, Massachusetts Institute of Technology, Cambridge, Massachusetts 02139, USA

<sup>6</sup>Quantum Technology Center, University of Maryland, College Park, Maryland 20742, USA

<sup>7</sup>Department of Electrical and Computer Engineering, University of Maryland, College Park, Maryland 20742, USA

<sup>8</sup>Department of Physics, University of Maryland, College Park, Maryland 20742, USA

 (Received 10 December 2019; revised 9 March 2020; accepted 27 April 2020; published 6 July 2020)

We introduce a microwave-assisted spectroscopy technique to determine the relative ratio of fluorescence emitted by nitrogen-vacancy (N-V) centers in diamond that are negatively charged (N-V<sup>-</sup>) and neutrally charged (N-V<sup>0</sup>) and present its application to studying spin-dependent ionization in N-V ensembles and enhancing N-V-magnetometer sensitivity. Our technique is based on selectively modulating the N-V<sup>-</sup> fluorescence with a spin-state-resonant microwave drive to isolate, *in situ*, the spectral shape of the N-V<sup>-</sup> and N-V<sup>0</sup> contributions to an N-V-ensemble sample's fluorescence. As well as serving as a reliable means to characterize the charge state, the method can be used as a tool to study spin-dependent ionization in N-V ensembles. As an example, we apply the microwave technique to a high-N-V-density diamond sample and find evidence for an additional spin-dependent ionization pathway, which we present here alongside a rate-equation model of the data. We further show that our method can be used to enhance the contrast of optically detected magnetic resonance (ODMR) on N-V ensembles and may lead to significant sensitivity gains in N-V magnetometers dominated by technical noise sources, especially where the N-V<sup>0</sup> population is large. With the high-N-V-density diamond sample investigated here, we demonstrate an up to 4.8-fold enhancement in the ODMR contrast. We also propose a second postprocessing method of increasing the ODMR contrast in shot-noise-limited applications. The techniques presented here may also be applied to other solid-state defects, as long as their fluorescence can be selectively modulated by means of a microwave drive. We demonstrate this utility by applying our method to isolate room-temperature spectral signatures of the V2-type silicon vacancy from an ensemble of V1 and V2 silicon vacancies in 4H silicon carbide.

DOI: [10.1103/PhysRevApplied.14.014009](https://doi.org/10.1103/PhysRevApplied.14.014009)

### I. INTRODUCTION

Ensembles of negatively charged nitrogen-vacancy centers (N-V<sup>-</sup>) in diamond are now a leading modality for

magnetic field sensing and imaging with high spatial resolution [1–3]. Importantly for diverse applications, N-V-diamond magnetometers can operate at ambient conditions and in direct contact with samples that are incompatible with the pressures or temperatures required in atomic or superconducting quantum interference device (SQUID) magnetometry, such as living organisms [4–7], paleomagnetic rocks [8,9], and temperature-dependent magnetic spin textures and current distributions [3].

However, the sensitivity of ensemble nitrogen-vacancy (N-V) diamond magnetometers, currently at approximately 1 pT/√Hz [10,11], still lags behind that of other methods, in part due to the presence of neutrally charged N-V/s

\*dianaplaude@g.harvard.edu

†Present address: Department of Physics and Research Laboratory of Electronics, Massachusetts Institute of Technology, Cambridge, Massachusetts 02139, USA

‡Present address: Sandia National Laboratories, Albuquerque, NM 87123, USA

§Present address: Lincoln Laboratory, Massachusetts Institute of Technology, Lexington, Massachusetts 02421, USA

( $N-V^0$ ) in diamond samples. Unlike the negatively charged defect, which exhibits spin-dependent optical behavior that can be used to prepare and read out its spin state [Fig. 1(a)] via optically detected magnetic resonance (ODMR), the neutral defect lacks a demonstrated optical method for spin-state preparation and readout. Hence, it cannot be used to optically measure and map magnetic fields.

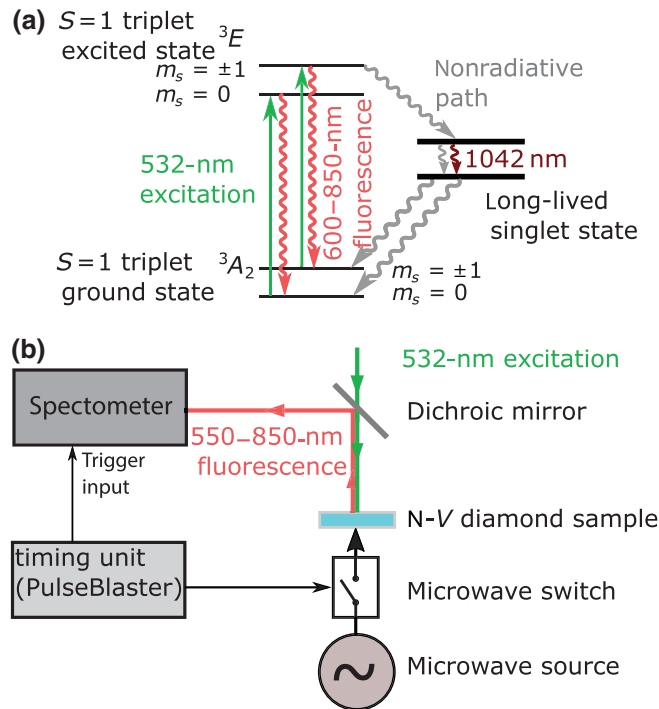


FIG. 1. (a) The  $N-V^-$  energy level structure, which enables ODMR. Under 532-nm illumination, the population in the  $m_s = 0$  state cycles in a spin-conserving transition between the ground state and the  ${}^3E$  excited state, fluorescing brightly when returning to the ground state. In contrast, the population in  $m_s = \pm 1$  appears dimmer, since it has an approximately 50% probability of nonradiatively crossing to a metastable singlet state, from whence it decays to the ground state—with slightly higher probability to the  $m_s = 0$  spin state—without emitting visible photons [12]. Hence, continuous 532-nm illumination will optically pump population to the  $m_s = 0$  state and a microwave drive resonant with the  $m_s = 0$  to  $m_s = \pm 1$  transition will modulate the fluorescence emitted by  $N-V^-$  by transferring population between the two spin states. (b) The experimental setup: a confocal microscope is used to illuminate a spot on an  $N-V$  diamond sample and to collect its fluorescence, which is directed to a spectrometer by a dichroic mirror. A computer-controlled timing unit (Spincore PulseBlaster card), controlled by an extended version of the software package qdSpectro [13], is used to trigger the acquisition of spectra and to control a microwave switch, which turns on and off a 2.87-GHz microwave drive delivered to the diamond via a microwave stripline board. Once triggered, the spectrometer acquires data for an exposure time  $t_{\text{exp}}$ , typically set at 30 ms, during which time a photoluminescence (PL) spectrum is acquired.

Instead, under illumination with the 532-nm light typically used for ODMR of  $N-V^-$  ensembles,  $N-V^0$  defects produce only a spin-independent fluorescence background, which degrades the readout contrast of the  $N-V^-$  spin state, reducing the magnetic field sensitivity.

Material properties relating to diamond growth and processing are thought to impact the relative concentrations of  $N-V^0$  and  $N-V^-$  defects in a given sample and these must be optimized to yield diamond samples with the best magnetic sensitivity [14]. Further, there is evidence that  $N-V^0$  can recombine with electrons in the lattice to form  $N-V^-$  and that  $N-V^-$  can ionize to  $N-V^0$ , with recombination and ionization rates depending on both the wavelength and intensity of the laser illumination [14–18].

The development of new methods to characterize and tune the steady-state charge state of  $N-V$  ensembles in diamond is therefore crucial. A better understanding of charge-state physics in dense  $N-V$  ensembles will lead to improved sensitivity of  $N-V$  magnetometers, which will in turn allow us to investigate and image a wider range of magnetic phenomena in condensed-matter physics, biophysics, and chemistry [11, 19–22].

In particular, there is a need for a charge-state-determination method that does not require the application of a specified illumination sequence but functions, instead, under any experimental conditions. Such a method can be used to determine what the charge-state ratio will be when any given experimental protocol of interest is applied. Furthermore, it has been previously observed that features of the fluorescence spectra of  $N-V^-$  and  $N-V^0$  defects change both as a function of the experimental parameters, such as the temperature [23] and the illumination wavelength [14], and the material properties, such as the local strain [24]; suggesting that spectra taken from such defects in different samples, or even from different locations in the same sample, may not be comparable. Such variations in spectra are not accounted for in many currently used methods for charge-state determination, such as taking the ratio of the areas under the  $N-V^0$  and  $N-V^-$  zero-phonon lines (ZPLs) in an  $N-V$ -ensemble photoluminescence (PL) spectrum or using single- $N-V$  spectra reported in the literature to fit for the  $N-V^-$  and  $N-V^0$  contributions in another sample's spectrum, making it difficult to compare measurements made by different experiments.

In this paper, we demonstrate a simple microwave-assisted spectroscopy method for determination of the steady-state charge-state in an  $N-V$  ensemble. Our method extracts the  $N-V^-$  and  $N-V^0$  spectra of the ensemble of interest *in situ*, accounting for any variations due to the local environment or experimental conditions. The microwave technique does not rely on a specific illumination sequence and can be applied with any laser excitation that produces a fluorescence contrast between the  $m_s = 0$  and  $m_s = \pm 1$  spin states of  $N-V^-$ . It may thus be used to investigate how illumination conditions, material

properties, and other experimental parameters affect the charge state in an N- $V$  ensemble.

Additionally, our method provides a useful tool to study spin-dependent ionization in N- $V$  ensembles. As an example, we apply the technique to reveal an additional spin-dependent N- $V$  ionization mechanism in a high-N- $V$ -density diamond sample. The microwave method can also provide a better understanding of N- $V$  ionization dynamics. This is useful not only to establish ideal operating conditions for N- $V$  ensemble magnetometers, which require a large stable population of N- $V^-$  defects, but also to expand the applicability of N- $V$  spin readout techniques that rely on spin-to-charge conversion.

We further demonstrate that our method can be used to perform background-free ODMR on N- $V^-$  defects by effectively suppressing the background fluorescence from the N- $V^0$  population to restore the ODMR contrast. We present two variations of the microwave technique that can be used to enhance contrast in ODMR magnetometry with N- $V$  ensembles in diamond. The first variation is a fitting method that applies microwave-modulated spectroscopy to identify and select only the N- $V^-$  fluorescence contribution in ODMR measurements. This method allows us to retrieve the N- $V^-$ -only ODMR line shape, restoring contrast. We find that, for ensemble N- $V$  magnetometers limited by laser-intensity noise, this method can offer significant improvements in contrast. Our simulations indicate that, even at modest intensity-noise levels of 1%, the ODMR contrast can be improved by up to 2 orders of magnitude, with the largest improvements in N- $V^0$ -rich ensembles. Such ensembles occur both in highly irradiated diamonds and near a diamond's surface, where the energetically preferable charge state is N- $V^0$  [25]. Increasing the contrast in the latter category of N- $V$  ensemble is of particular importance in magnetometry applications that require sensor N- $V$ s to be very close to the measured sample.

The second method of contrast enhancement involves postprocessing wavelength-discriminated N- $V$  fluorescence data by preferentially weighting up wavelength bins expected to contain larger fractions of N- $V^-$  photons. The function used to perform the weighting is determined based on the N- $V^-$  and N- $V^0$  spectral shapes extracted using our microwave-modulation method and is tailored to a given diamond sample. This tailored-weighting technique is applicable to shot-noise-limited magnetometers but offers comparably more modest contrast improvements of up to approximately 50%.

Finally, we show how our method may be applied to study spectral properties of other solid-state defects. By modulating a radio-frequency (rf) drive applied to a room-temperature ensemble of V1 and V2 vacancies in 4H silicon carbide, we isolate spectral signatures of the V2 vacancy that would not typically be discernible at room temperature, since the two vacancies exhibit overlapping spectra.

Section II of this paper describes our method of charge-state determination in detail. Section III outlines the method's applications beyond charge-state determination and presents pilot experiments applying the method to study spin-dependent ionization in N- $V$  ensembles, to perform high-contrast ODMR, and to isolate spectral features of fluorescent defects in other solid-state systems. Finally, Sec. IV discusses our conclusions.

## II. METHOD

Our method centers around isolating the N- $V^-$ - and N- $V^0$ -fluorescence contributions to the photoluminescence spectrum emitted by an ensemble of N- $V$ s by selectively modulating the N- $V^-$  fluorescence with a microwave drive. We can write the spectrum measured in the absence of a microwave drive, which we will henceforth call the microwaves-off spectrum,  $S_{\text{MWoff}}(\lambda)$ , in terms of an N- $V^-$  and an N- $V^0$  component, as follows:

$$S_{\text{MWoff}}(\lambda) = a_{\text{N-}V^-} \hat{S}_{\text{N-}V^-}(\lambda) + a_{\text{N-}V^0} \hat{S}_{\text{N-}V^0}(\lambda), \quad (1)$$

where  $\hat{S}_{\text{N-}V^-}(\lambda)$  and  $\hat{S}_{\text{N-}V^0}(\lambda)$  are the intensity-normalized N- $V^-$  and N- $V^0$  spectra, normalized to have unit area (one can think of these as basis spectra) and  $a_{\text{N-}V^-}$ ,  $a_{\text{N-}V^0}$  are positive constants, representing the area under the N- $V^-$  and N- $V^0$  contributions to the total microwaves-off spectrum.

We focus on quantifying the N- $V^-$ -to-N- $V^0$  fluorescence intensity ratio, which is closely related to the N- $V^-$  fluorescence contrast figure of merit for N- $V$  magnetometry. The fluorescence intensity ratio is related to the true N- $V^-$ -to-N- $V^0$  charge-state ratio, which one can extract given the pump-absorption cross sections, the excited-state fluorescence lifetimes, and a rate-equation model for the steady-state populations.

Our goal is hence to decompose the total microwaves-off spectrum into its N- $V^-$  and N- $V^0$  contributions:

$$\begin{aligned} S_{\text{N-}V^-}(\lambda) &= a_{\text{N-}V^-} \hat{S}_{\text{N-}V^-}(\lambda), \\ S_{\text{N-}V^0}(\lambda) &= a_{\text{N-}V^0} \hat{S}_{\text{N-}V^0}(\lambda), \end{aligned} \quad (2)$$

from which we can determine the ratio of areas,  $a_{\text{N-}V^-}/a_{\text{N-}V^0}$ . This involves three main steps:

1. Isolate the N- $V^-$  spectral shape by microwave modulation.
2. Find the correct scale factor by which to multiply the spectral shape of N- $V^-$ , to determine the total N- $V^-$  contribution to  $S_{\text{MWoff}}(\lambda)$ .
3. Correct for spin-dependent ionization.

Finding the absolute charge-state ratio will also require measuring the radiative lifetimes  $\tau_{\text{N-}V^0}$  and  $\tau_{\text{N-}V^-}$  (which can be done using time-correlated photon counting, as previously demonstrated in [26], for example) and calibrating

out the effect of any wavelength-dependent losses in the optics setup (using, for instance, a white-light source). The subsections that follow describe each of the steps for determining  $a_{N-V^-}/a_{N-V^0}$  in detail and present an example application to photoluminescence data taken at a confocal spot on a bulk N-V ensemble in a chemical-vapor-deposition-grown diamond sample. Further details on our diamond sample and our confocal setup are given in the Appendix, Sec. A 1.

### A. Isolating the N- $V^-$ spectral shape by microwave modulation

A series of photoluminescence spectra is taken under continuous 532-nm illumination, with alternating spectra taken with microwaves on and off [as described in the caption to Fig. 1(b)]. To select the microwave-drive frequency at which we operate, we take an ODMR spectrum before acquiring the series of PL spectra and set the microwave frequency to be resonant with one of the N- $V^-$  magnetic sublevel transition frequencies.

In our example demonstration, we work at zero applied magnetic field (but do not cancel the Earth's field), where the splitting in energy between  $m_s = +1$  and  $m_s = -1$  spin states is small (here, a few megahertz) and predominantly caused by local effects (most likely random local electric fields, as discussed in Ref. [27]). Due to the absence of a sufficiently strong magnetic field, the ODMR resonances of all N- $V^-$  orientations are near degenerate and all orientations are hence addressed by our strong microwave drive (with a Rabi frequency of approximately a few megahertz). Note, however, that with an applied magnetic field oriented such that it splits the ODMR lines of different N- $V^-$  orientations, our method can also be used to selectively determine the charge state of an ensemble of N- $V^-$ s oriented along one chosen axis.

When applied to the N- $V^-$  ensemble, the resonant microwave drive transfers population between the bright  $m_s = 0$  state and the dimmer  $m_s = \pm 1$  states, modulating the fluorescence emitted by N- $V^-$  while having no effect on N- $V^0$  fluorescence [Fig. 1(a)]. By taking the difference between successive PL spectra measured with microwaves on and off, it is hence possible to isolate the spectral shape of the N- $V^-$  contribution to the detected fluorescence. We define the difference spectrum,  $S_{\text{diff}}(\lambda)$ , as

$$S_{\text{diff}}(\lambda) = S_{M\text{Woff}}(\lambda) - S_{M\text{Won}}(\lambda), \quad (3)$$

where  $S_{M\text{Won}}(\lambda)$  and  $S_{M\text{Woff}}(\lambda)$  are the spectra taken with microwaves on and off, respectively, averaged over the series. Typically, between 2000 and 20 000 spectra are taken to average out the effect of shot-to-shot laser-intensity drift. This averaging, along with the use of a noise-eater circuit on the excitation path (Thorlabs NEL01), reduces the contribution of shot-to-shot intensity fluctuations to the difference spectrum to under 0.05%.

Once the difference spectrum is extracted, the N- $V^-$  and N- $V^0$  spectra can be written as

$$S_{N-V^-}^{\text{trial}}(\lambda; k) = k \times S_{\text{diff}}(\lambda), \quad (4)$$

$$\begin{aligned} S_{N-V^0}^{\text{trial}}(\lambda; k) &= S_{M\text{Woff}}(\lambda) - S_{N-V^-}^{\text{trial}}(\lambda; k) \\ &= S_{M\text{Woff}}(\lambda) - kS_{\text{diff}}(\lambda), \end{aligned} \quad (5)$$

where the ‘‘trial’’ superscript denotes that these are not the final spectral shapes, as they will later be modified by a correction for spin-dependent ionization (Sec. II C) and  $k$  denotes a scale factor, to be determined in Sec. II B. Note that  $k$  cannot simply be determined by measuring the N- $V^-$  ODMR contrast because, without knowledge of the ratio of charge-state concentrations in the spot being illuminated, it is not possible to determine by how much we dim the N- $V^-$  fluorescence when the microwaves are turned on (we

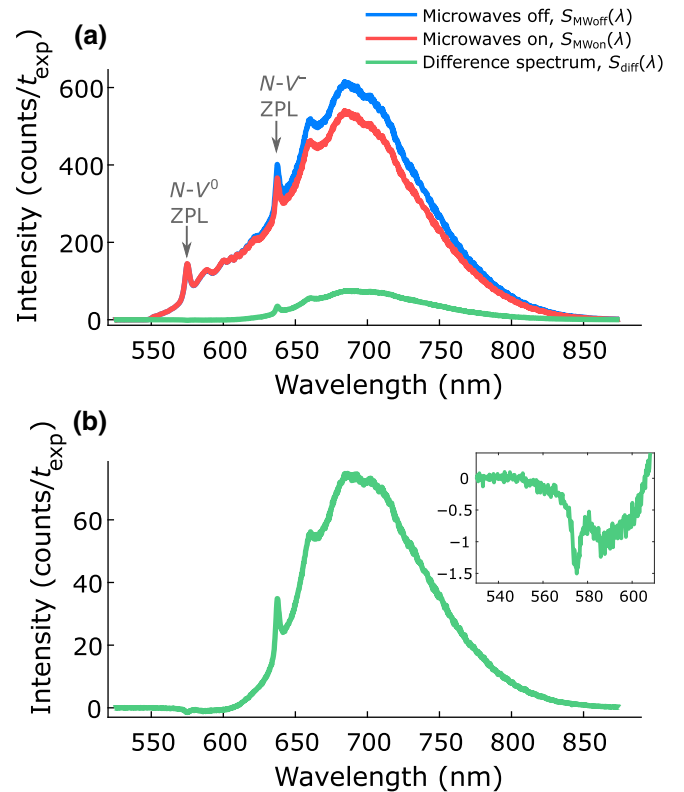


FIG. 2. (a) Measured microwaves-on (red) and microwaves-off (blue) PL spectra with both the N- $V^0$  and N- $V^-$  zero-phonon lines (indicated by gray arrows) visible at 575 nm and 637 nm, respectively. The unscaled difference spectrum (microwaves off – microwaves on) is shown in green. (b) A magnified view of the difference spectrum, composed mostly of N- $V^-$  fluorescence, except for a small N- $V^0$  contribution due to a spin-dependent ionization effect, which causes a negative N- $V^0$  ZPL signature. An enlarged view of this N- $V^0$  ZPL signature is shown in the inset on the top right. The spin-dependent ionization effect is corrected for in Sec. II C and discussed further in Sec. III A.

can only establish by how much we dim the total fluorescence). The measured difference spectrum of our example N- $V^-$  ensemble is shown in Fig. 2.

### B. Finding the correct scale factor

We can now iterate the scale factor  $k$  and examine the resulting N- $V^0$  spectra,  $S_{N-V^0}^{\text{trial}}(\lambda; k)$ , that we obtain by evaluating Eq. (5) for each value of  $k$ . Since the N- $V^-$  ZPL at 637 nm is a defining feature of the N- $V^-$  emission spectrum that should not appear in the N- $V^0$  spectrum, we can find the correct scale factor  $k$  by minimizing the area under any residual N- $V^-$  ZPL feature in  $S_{N-V^0}^{\text{trial}}(\lambda; k)$  (Fig. 3). We first find the width and center wavelength of the N- $V^-$  ZPL by fitting the N- $V^-$  ZPL on the microwaves-off spectrum with a Gaussian line shape on a polynomial background.

We then scan  $k$  and fit  $S_{N-V^0}^{\text{trial}}(\lambda; k)$  for a Gaussian feature of the same width and center wavelength as the N- $V^-$  ZPL; we select  $k = k_0$ , where  $k_0$  minimizes the area,  $A$ , under this Gaussian, i.e.,  $A(k_0) = \min(A(k))$  [Figs. 3(b) and 3(c)]. From Eqs. (4) and (5), we can now evaluate trial N- $V^-$  and N- $V^0$  spectra,  $S_{N-V^-}^{\text{trial}}(\lambda, k_0)$  and  $S_{N-V^0}^{\text{trial}}(\lambda, k_0)$ .

### C. Correcting for spin-dependent ionization

The N- $V^- \rightarrow$  N- $V^0$  ionization rate may be different when microwaves are on and off (see Sec. III A). This is because the microwave drive will modify the steady-state distribution of population across the N- $V^-$  energy levels and hence the rate at which population can be transferred to N- $V^0$ . For example, with microwaves on, a larger fraction of the population will be transferred to the long-lived

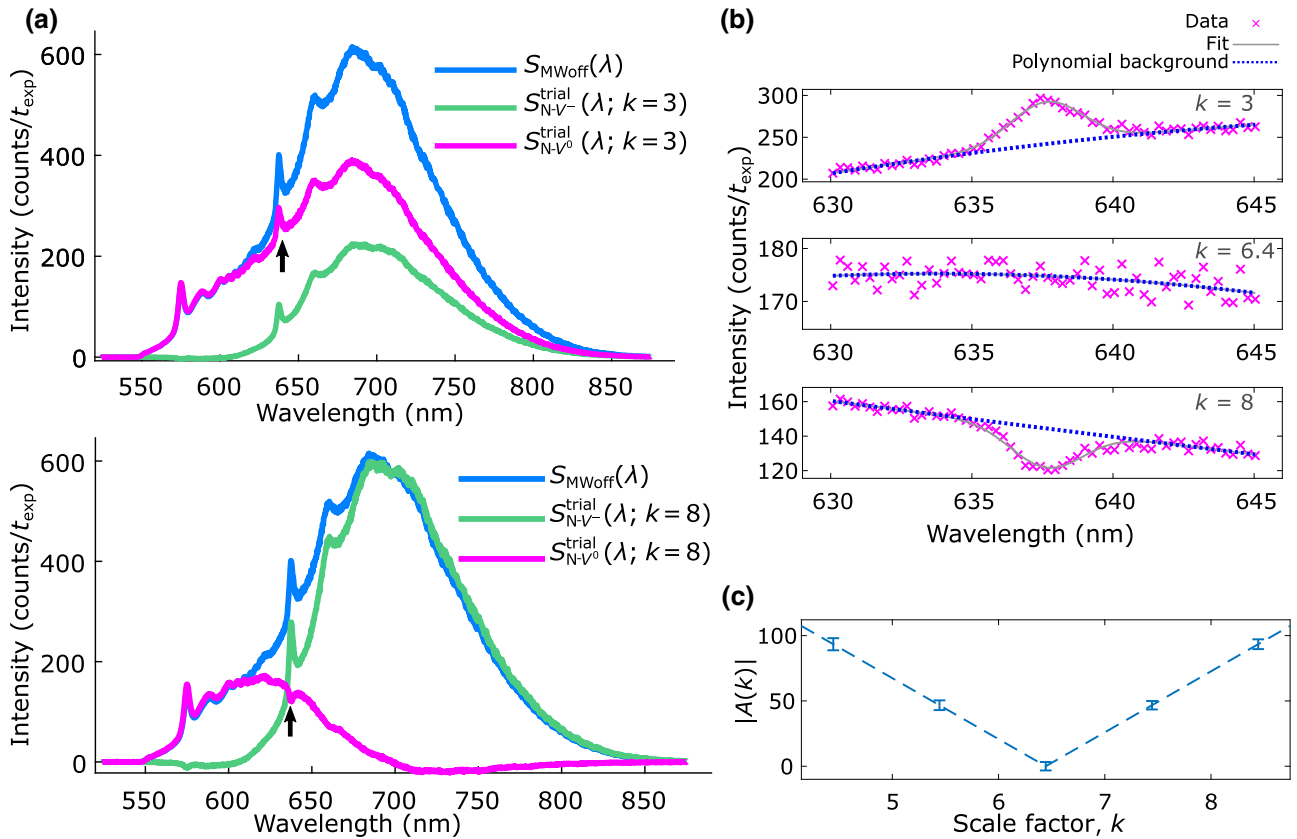


FIG. 3. The difference spectrum must be scaled by an unknown factor,  $k$ , to yield the N- $V^-$  contribution to the spectrum,  $S_{N-V^-}^{\text{trial}}(\lambda; k) = kS_{\text{diff}}(\lambda)$ . The extracted N- $V^0$  spectrum, found by subtracting the N- $V^-$  spectrum from the total microwaves-off spectrum,  $S_{N-V^0}^{\text{trial}}(\lambda; k) = S_{\text{MWO}}(\lambda) - kS_{\text{diff}}(\lambda)$ , should contain no N- $V^-$  ZPL signature at 637 nm when the scale factor  $k$  is chosen correctly.

(a) The total measured PL spectrum (blue) and trial N- $V^-$  (green) and N- $V^0$  (magenta) spectra for scale factors  $k = 3 \ll k_0$  (top) and  $k = 8 \gg k_0$  (bottom), where  $k_0$  is the correct scale factor (for the N- $V^-$  ensemble analyzed here,  $k_0 = 6.4$ ). For  $k$  smaller (larger) than the correct value  $k_0$ , a peak (dip) is seen in the extracted N- $V^0$  spectrum at the N- $V^-$  ZPL wavelength, as indicated by the black arrows.

(b) The trial N- $V^0$  spectrum (magenta crosses) in the wavelength range around the N- $V^-$  ZPL is fitted with a Gaussian line shape on a polynomial background (total fit function shown as solid line in gray and polynomial background shown as a dotted line in blue) for  $k = 3 \ll k_0$  (top),  $k = k_0 = 6.4$  (middle), and  $k = 8 \gg k_0$  (bottom). Of the Gaussian's fit parameters, only the area,  $A(k)$ , is allowed to vary, since the width and center are fixed to match those of the N- $V^-$  ZPL.

(c) The fitted area under the Gaussian peak or dip,  $|A(k)|$  as a function of the scale factor  $k$ . The area is minimized at the correct scale factor,  $k = k_0 = 6.4$ .

singlet state, or “shelf,” under green illumination. A different ionization rate for microwaves on and off leads to a small change in the steady-state  $N-V^0$  population, which in turn produces an  $N-V^0$  signature in the difference spectrum: e.g., if the ionization rate is larger with microwaves on than off, there will be a larger  $N-V^0$  population when the microwaves are on, leading to a negative  $N-V^0$  contribution to the difference spectrum. For the purposes of charge-state determination, we must correct for this signature in order to retrieve the shape of the pure- $N-V^-$  spectrum. However, it is important to note that this signature can also be used as a tool to study spin-dependent ionization in  $N-V$  ensembles—in particular, the sign of the  $N-V^0$  signature in the difference spectrum indicates whether microwaves promote or suppress  $N-V^-$  ionization and can reveal, as shown in Sec. III A, additional ionization pathways.

For the data set analyzed here, the  $N-V^0$  concentration is boosted when the microwave drive is on due to sublevel-dependent  $N-V^-$  photoionization (a process we model in Sec. III A). This causes the difference spectrum  $S_{\text{diff}}(\lambda) = S_{\text{MWoff}}(\lambda) - S_{\text{MWon}}(\lambda)$  to have a small negative contribution from the  $N-V^0$  spectrum, as can be seen in Fig. 4(a). Note, however, that the  $N-V^0$  spectrum that we extract in

Sec. II B,  $S_{N-V^0}^{\text{trial}}(\lambda, k_0)$ , consists purely of  $N-V^0$  fluorescence by definition, since we select the scale factor  $k_0$  that eliminates any  $N-V^-$  signature in the  $N-V^0$  spectrum. To see this, we can rewrite the difference spectrum as

$$S_{\text{diff}}(\lambda) = cS_{N-V^-}(\lambda) - \delta S_{N-V^0}(\lambda), \quad (6)$$

where  $c$  and  $\delta$  are scalar positive constants and  $S_{N-V^0}(\lambda)$ ,  $S_{N-V^-}(\lambda)$  are the  $N-V^0$  and  $N-V^-$  components of the microwaves-off spectrum, as defined in Eq. (2). Then, the trial  $N-V^0$  spectrum that we extract in Sec. II B can be written as

$$\begin{aligned} S_{N-V^0}^{\text{trial}}(\lambda; k_0) &= S_{\text{MWoff}} - k_0 S_{\text{diff}}(\lambda) \\ &= (1 + k_0 \delta) S_{N-V^0}(\lambda) \\ &\quad + (1 - k_0 c) S_{N-V^-}(\lambda). \end{aligned} \quad (7)$$

Note, however, that we choose  $k = k_0$  such that there is no  $N-V^-$  contribution in  $S_{N-V^0}^{\text{trial}}$ , i.e.,  $(1 - k_0 c) = 0$ . Hence,

$$S_{N-V^0}^{\text{trial}}(\lambda; k_0) = (1 + k_0 \delta) S_{N-V^0}(\lambda). \quad (8)$$

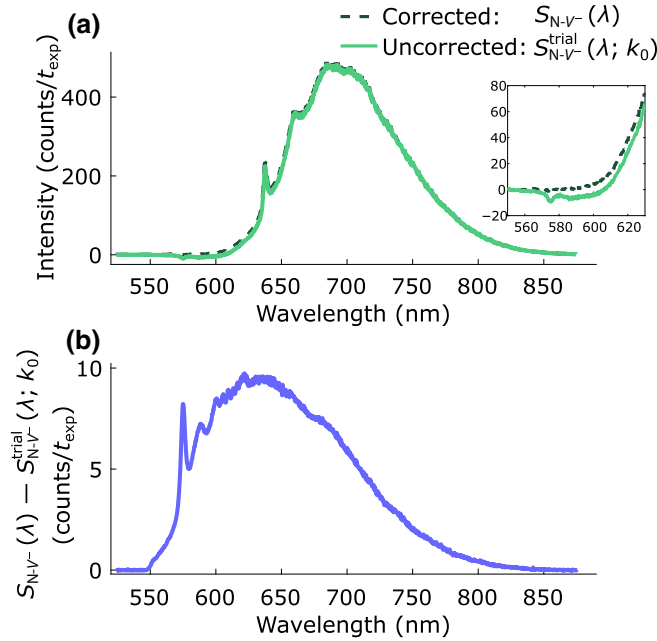


FIG. 4. (a) The trial  $N-V^-$  PL spectrum,  $S_{N-V^-}^{\text{trial}}$ , before correction for spin-dependent ionization (light green solid line), and the corrected  $N-V^-$  spectrum,  $S_{N-V^-}$  (dark green dashed line). The inset shows the spectrum plotted in the wavelength range around the  $N-V^0$  ZPL. (b) The difference between the corrected and uncorrected  $N-V^-$  spectra [ $S_{N-V^-}(\lambda) - S_{N-V^-}^{\text{trial}}(\lambda; k_0)$ ]. Qualitatively, most of the contribution to this difference appears to come from  $N-V^0$  fluorescence—note the prominent peak at the  $N-V^0$  ZPL wavelength.

We can therefore correct  $S_{N-V^0}^{\text{trial}}(\lambda; k_0)$  simply by rescaling it to match the microwaves-off spectrum in the wavelength region where only  $N-V^0$  fluoresces (below 585 nm); i.e., we effectively divide  $S_{N-V^0}^{\text{trial}}(\lambda; k_0)$  by  $(1 + k_0 \delta)$  to obtain the correct  $N-V^0$  spectrum,  $S_{N-V^0}(\lambda)$ . Note that we can also perform this rescaling by multiplying  $S_{N-V^0}^{\text{trial}}(\lambda; k_0)$  by the ratio of the fitted areas of the  $N-V^0$  ZPL in the microwaves-off spectrum and in  $S_{N-V^0}^{\text{trial}}(\lambda; k_0)$ —we find that these two rescaling methods agree within uncertainties.

Finally, we subtract the corrected  $N-V^0$  spectrum from the total microwaves-off spectrum to yield a corrected  $N-V^-$  spectrum,  $S_{N-V^-}(\lambda) = S_{\text{MWoff}}(\lambda) - S_{N-V^0}(\lambda)$ . Figure 4 plots both the corrected and trial  $N-V^-$  spectra,  $S_{N-V^-}(\lambda)$  and  $S_{N-V^-}^{\text{trial}}(\lambda; k_0)$ , for our example  $N-V$ -ensemble data. Figure 5 plots the  $N-V$  ensemble’s spectral decomposition into  $N-V^-$  and  $N-V^0$  fluorescence contributions: 69(1)%  $N-V^-$  and 31(1)%  $N-V^0$ .

As presented here, our  $N-V$  charge-state determination method assumes that the main contributions to the fluorescence in the diamond are  $N-V^-$  and  $N-V^0$  defects. Modifications including the addition of microwave modulation at other frequencies (to distinguish other spin-dependent fluorescence) may be required to successfully apply this method to diamonds containing significant populations of other defects that fluoresce in an overlapping spectral range. In Sec. III C, we demonstrate the application of a simplified version of this method using modulation at radio frequencies to extract spectral features of silicon vacancies in silicon carbide.

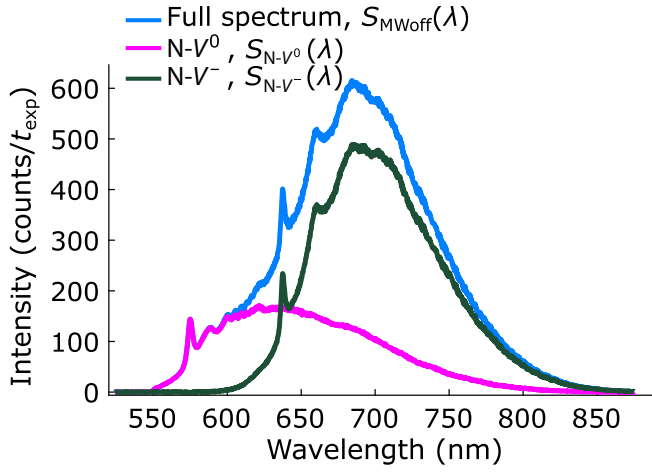


FIG. 5. The spectral decomposition (for our measurement and illumination conditions) of a measured N- $V$ -ensemble PL spectrum (blue) into an N- $V^-$  contribution,  $S_{N-V^-}(\lambda)$  (dark green) and an N- $V^0$  contribution,  $S_{N-V^0}(\lambda)$  (magenta). From the area under  $S_{N-V^0}(\lambda)$  and  $S_{N-V^-}(\lambda)$ , we establish that 69(1)% of the fluorescence of this N- $V$  ensemble is contributed by N- $V^-$  defects and 31(1)% by N- $V^0$  defects.

### III. APPLICATIONS

In this section, we discuss applications of the microwave-assisted spectroscopy technique as a tool to study spin-dependent ionization in N- $V$  ensembles, as a means of increasing the ODMR contrast in N- $V$  magnetometers and as a method for isolating spectral signatures of other solid-state defects that exhibit spin-dependent fluorescence contrasts.

#### A. Studying spin-dependent ionization: postulated ionization transition pathway

The fact that the rate of ionization from N- $V^-$  to N- $V^0$  under 532-nm illumination depends on the spin state of N- $V^-$  is well documented in the literature [28–30]. Currently, the spin dependence of N- $V^-$  ionization is postulated to arise from the preferential transfer of the  $m_s = \pm 1$  state to the singlet “shelf” state. It is assumed that this shelf state protects the population from ionization driven by the green light, which is instead taken to occur mainly via transitions from the excited triplet state.

However, at powers above a few microwatts of green light, we observe the opposite effect. The N- $V^-$  ionization probability for our N- $V$  ensemble is enhanced when the microwaves are on, indicating that the  $m_s = \pm 1$  state is preferentially ionized. This is manifested, as shown in Fig. 2b and Fig. 4, as a negative N- $V^0$  fluorescence contribution to the difference spectrum, arising from an increase in N- $V^0$  fluorescence in the microwaves-on spectrum, compared to that in the microwaves-off spectrum.

To further investigate this effect, we measure the microwave-induced modulation of N- $V^0$  fluorescence in our sample at several different applied 532-nm laser powers, ranging from 10  $\mu$ W to a few milliwatts. At each laser power, a series of 10 000 microwaves-on and microwaves-off spectra (each with 30-ms exposure time) are recorded, from which an average difference spectrum is determined (following the same method as described in Sec. II A). The area under the N- $V^0$  ZPL of this difference spectrum is fitted and divided by the area under the N- $V^0$  ZPL of the averaged microwaves-off spectrum, to give a measure of the N- $V^0$  contrast. This gives a measure of the difference in the N- $V^0$  population when the microwaves are on and off as a fraction of (or normalized to) the N- $V^0$  population when the microwaves are off. Note that this N- $V^0$  contrast could have also been determined by decomposing both microwaves-on and microwaves-off spectra into their N- $V^0$  and N- $V^-$  component spectra and evaluating the difference in total N- $V^0$  counts (integrated over all wavelengths) in the microwaves-on and microwaves-off spectra (as a fraction of the total N- $V^0$  counts in the microwaves-off spectrum). Here, we instead evaluate the N- $V^0$  contrast via the simpler procedure of measuring counts under the N- $V^0$  ZPL in the difference spectrum (normalized to counts under the N- $V^0$  ZPL in the microwaves-off spectrum) in order to minimize any potential systematics that could mix N- $V^-$  and N- $V^0$  counts; we do so to ascertain and show that the spin-dependent ionization effects observed here cannot have been caused by any potential systematics introduced by spectral decomposition analysis.

We emphasize that the microwave-induced N- $V^0$  fluorescence contrast we observe here does not arise from the modulation of the fluorescence rate of individual N- $V^0$  centers (N- $V^0$  does not exhibit spin-dependent fluorescence contrast) but, rather, from a change in the steady-state N- $V^0$  population in the ensemble. We plot the measured N- $V^0$  contrast versus the applied laser power in Fig. 6(a). We observe, for our N- $V$  ensemble, a negative fluorescence contrast (i.e., more N- $V^0$  population when microwaves are on) over the range of laser powers accessed here. This indicates that the application of microwaves is either enhancing ionization from N- $V^-$  to N- $V^0$  or suppressing recombination from N- $V^0$  to N- $V^-$ . Here, we postulate the existence of an ionization pathway from the N- $V^-$  singlet “shelf” states mediated by 532-nm light and show that such a pathway would lead to an enhanced N- $V^-$  ionization rate with the observed power dependence.

To model this mechanism, we develop a seven-level rate-equation model of the steady-state population dynamics in the N- $V$  ensemble, depicted schematically in Fig. 7. This model can be expressed as a set of simultaneous equations in matrix form, given in Eq. (9): a matrix of transition rates between levels acts on a vector of populations (with elements  $p_n$  representing the population of level  $n$ ).

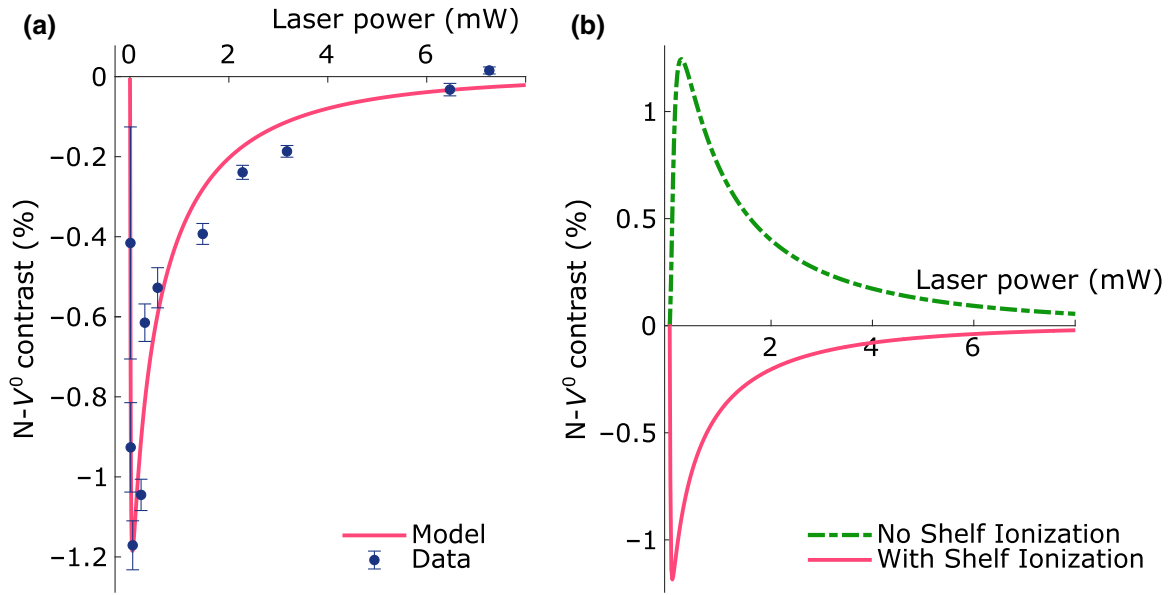


FIG. 6. (a) The measured  $N-V^0$  contrast versus the laser power (dark blue) and the rate-equation model fit (red curve). The negative contrast indicates that the overall  $N-V^-$  ionization rate increases when the microwaves are on. The model reproduces this effect by introducing a postulated ionization transition from the  $N-V^-$  singlet states (“shelf”), driven by the 532-nm laser. (b) The rate-equation model plotted with (red curve) and without (dashed green curve) the postulated ionization transition from the shelf. In the absence of the postulated ionization transition, the model, which uses literature values for established transition rates, predicts positive  $N-V^0$  contrast at all applied laser powers, in stark disagreement with the data. The rate-equation model is described in detail in the main text and in the Appendix (Sec. A 2).

$$\begin{pmatrix} -m_{12}-d_i-a_e P & m_{21} & k_{31} & 0 & k_{51} & \frac{1}{2}d_r & \frac{1}{2}a_r P \\ m_{12} & -m_{21}-a_e P-d_i & 0 & k_{42} & k_{52} & \frac{1}{2}d_r & \frac{1}{2}a_r P \\ a_e P & 0 & -k_{31}-k_{35}-a_i P & 0 & 0 & 0 & 0 \\ 0 & a_e P & 0 & -k_{42}-k_{45}-a_i P & 0 & 0 & 0 \\ 0 & 0 & k_{35} & k_{45} & -k_{51}-k_{52}-a_s P & 0 & 0 \\ d_i & d_i & a_i P & a_i P & a_s P & -a_0 P-d_r & k_{76} \\ 0 & 0 & 0 & 0 & 0 & a_0 P & -a_r P-k_{76} \end{pmatrix} \begin{bmatrix} p_1(P) \\ p_2(P) \\ p_3(P) \\ p_4(P) \\ p_5(P) \\ p_6(P) \\ p_7(P) \end{bmatrix} = 0. \quad (9)$$

The equality with zero indicates that we are interested in the steady-state solution where each level neither gains nor loses population. Solving this matrix equation with the constraint that  $\sum p_n = 1$  (i.e., the total population is constant) yields a power-dependent analytic function for the population of each level. To obtain the  $N-V^0$  contrast as a function of the applied laser power, we plot

$$N-V^0 \text{ contrast}(P) = \alpha \frac{p_7^{\text{MWoff}}(P) - p_7^{\text{MWon}}(P)}{p_7^{\text{MWoff}}(P)}, \quad (10)$$

where  $\alpha$  is a scale factor that we float in the fit to data and  $p_7^{\text{MWon}}(P)$  and  $p_7^{\text{MWoff}}(P)$  are, respectively, the steady-state population of the excited state of  $N-V^0$  with microwaves on and with microwaves off (i.e., with the microwave-driven transition rates set to zero) at the applied 532-nm laser power  $P$ .

Our model uses literature values for all transition rates except for the newly postulated ionization rate from the shelf. The transition rates used are listed in Table I and described in detail in the Appendix, Sec. A 3. We use our model to fit the data in Fig. 6(a) by keeping all parameters fixed to literature values and floating only the postulated ionization transition rate from the shelf, the  $N-V^-$  excitation rate, and an overall scale factor  $\alpha$  in Eq. (10). The model provides a good fit to the data [red curve in Fig. 6(a)] when the shelf-ionization transition is included. If this transition is removed (i.e.,  $a_s$  is set to 0), the model predicts positive contrast at all powers [dashed green curve in Fig. 6(b)], in stark disagreement with our data.

Our model’s good agreement with the data indicates the existence of an additional ionization pathway from the singlet states driven by 532-nm light, which warrants further investigation beyond the scope of the

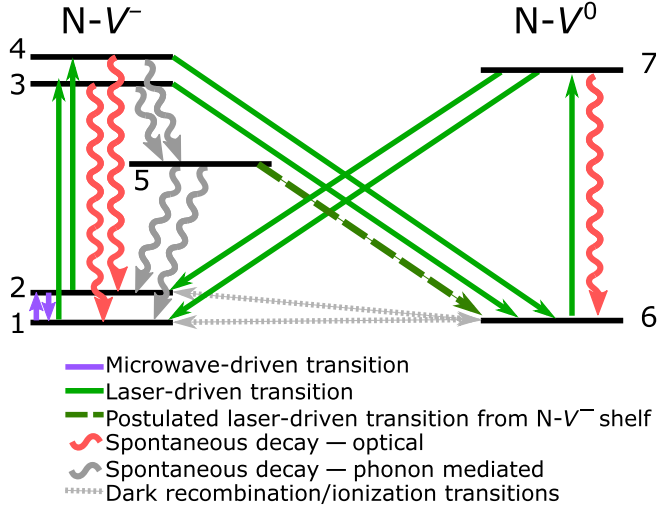


FIG. 7. The seven-level rate-equation model of the steady-state population dynamics in an N-V ensemble. N-V<sup>-</sup> is represented by five levels: the  $m_s = 0$  and  $m_s = \pm 1$  levels of the ground (levels 1 and 2) and excited (levels 3 and 4) triplet states and one level (level 5) representing the long-lived singlet shelf. N-V<sup>0</sup> is represented by two levels: a ground state (level 6) and an excited state (level 7). Ionization from N-V<sup>-</sup> to N-V<sup>0</sup> can occur either via a laser-driven transition from the excited states of N-V<sup>-</sup> (levels 3 and 4) or the postulated laser-driven transition (dashed green line) from the shelf (level 5). Recombination occurs via a laser-driven transition from the excited state of N-V<sup>0</sup> (level 7) to the ground state of N-V<sup>-</sup> (levels 1 and 2). Additionally, slow (approximately  $100 \mu\text{s}^{-1}$ ) dark ionization and recombination rates link the ground states of N-V<sup>-</sup> and N-V<sup>0</sup>.

present work. Indeed, the need for the introduction of new spin-dependent mechanisms of N-V<sup>-</sup> ionization has recently also been recognized by Reece *et al.* [31], who found that introducing an *ad hoc* spin dependence to the N-V<sup>-</sup> ionization rate from the triplet excited states produced a better fit to their data on charge-state interconversion in nanodiamonds. Further investigation of the postulated ionization transition from the singlet states could elucidate whether this is the mechanism behind the observed behavior. This would involve performing time-resolved spectroscopy on a variety of N-V diamond samples and under different microwave and laser-power regimes.

The ionization pathway proposed here may reveal pertinent considerations in spin-dependent ionization dynamics. An understanding of such dynamics is important in performing spin-to-charge readout [30,32] and could uncover potential avenues to enhance the steady-state N-V<sup>-</sup> population by diamond engineering.

## B. High-contrast ODMR

In N-V-based dc magnetometry, the Zeeman shift of either the  $m_s = +1$  or the  $m_s = -1$  energy levels of N-V<sup>-</sup>

TABLE I. The numerical values for the transition rates used in the rate-equation model [Eq. (9)] to fit the data plotted in Fig. 6. As described in the text, most rates are fixed to values taken from the literature, with the exception of the ones denoted by an asterisk (\*), which are determined from the fit to our data. Column 3 of this table describes the transitions to which each rate refers, with level numbering as depicted in Fig. 7.

Rate	Numerical value	Description
$m_{12}$	$3.1 \times 10^{-3} \text{ ns}^{-1}$	Microwave-driven rates between levels $1 \leftrightarrow 2$
$m_{21}$	$3.1 \times 10^{-3} \text{ ns}^{-1}$	
$k_{31}$	$7.5 \times 10^{-2} \text{ ns}^{-1}$	Spontaneous decay rates, $k_{nm}$ , between levels $n \rightarrow m$
$k_{42}$	$1.5 \times 10^{-1} \text{ ns}^{-1}$	
$k_{35}$	$1.1 \times 10^{-2} \text{ ns}^{-1}$	
$k_{45}$	$8.0 \times 10^{-2} \text{ ns}^{-1}$	
$k_{51}$	$2.6 \times 10^{-3} \text{ ns}^{-1}$	
$k_{52}$	$2.3 \times 10^{-3} \text{ ns}^{-1}$	
$k_{76}$	$5.0 \times 10^{-2} \text{ ns}^{-1}$	
$d_i$	$100 \mu\text{s}^{-1}$	Dark ionization: $1 \rightarrow 6, 2 \rightarrow 6$
$d_r$	$300 \mu\text{s}^{-1}$	Dark recombination: $6 \rightarrow 1, 6 \rightarrow 2$
$a_e^*P$	$5.9 \times 10^{-5} P \text{ ns}^{-1}$	Laser-driven rates, $a_x P$ , where $P$ is the laser power in microwatts
$a_0P$	$1.3 \times a_e P$	N-V <sup>-</sup> excitation: $1 \rightarrow 3, 2 \rightarrow 4$
$a_iP$	$0.037 \times a_e P$	N-V <sup>0</sup> excitation: $6 \rightarrow 7$
$a_rP$	$0.8 \times a_e P$	Ionization: $3 \rightarrow 6, 4 \rightarrow 6$
$a_s^*P$	$0.36 \times a_e P$	Recombination: $7 \rightarrow 1, 7 \rightarrow 2$
		Postulated shelf ionization: $5 \rightarrow 6$

is probed to determine the applied magnetic field. This is typically done by ODMR, whereby the frequency of a microwave drive is scanned over the  $m_s = 0$  to  $m_s = \pm 1$  resonance while the N-V is illuminated with 532-nm light. The 532-nm light optically pumps the N-V<sup>-</sup> population to  $m_s = 0$ , but when the microwaves are resonant with the  $m_s = 0$  to  $m_s = +1$  (or  $m_s = -1$ ) transition, some population is transferred from the bright  $m_s = 0$  state to the dimmer  $m_s = +1$  ( $m_s = -1$ ) state, causing a drop in N-V<sup>-</sup> fluorescence. This leads to a fluorescence contrast between resonant and off-resonant microwaves. The highest magnetic-field sensitivity is attained if one drives the N-V<sup>-</sup> at a microwave frequency on the side of the ODMR line, where the change in fluorescence per unit change in magnetic field is maximized—i.e., the point of largest slope in the ODMR line. The minimum field that can be sensed is inversely proportional to this slope. Hence, increasing the ODMR contrast (without broadening the ODMR line) leads directly to an increase in sensitivity.

In this section, we describe two methods of enhancing the ODMR contrast using the microwave-assisted charge-state-determination technique. The first method entails fitting N-V-ensemble spectra to extract only the N-V<sup>-</sup> fluorescence component; the second method involves postprocessing the ensemble's fluorescence data using a tailored weighting function determined *a priori*. The two methods

will henceforth be referred to as the *fitting method* and the *tailored-weighting method* respectively. In this section, we compare the performance of these methods with the traditional way of determining ODMR contrast, referred to here as *undiscriminated contrast*, which involves simply taking the difference in total counts emitted by an N- $V$  ensemble with microwaves on and microwaves off as a fraction of the total microwaves-off counts.

### 1. Fitting method

Any population of N- $V^0$  defects in an N- $V$  ensemble will degrade the ODMR contrast by contributing a spin-independent fluorescence background and, in turn, reduce the magnetic-field sensitivity of any measurements made with the N- $V$  ensemble. Using our charge-state-determination method, we can discard N- $V^0$  fluorescence and extract the N- $V^-$ -only ODMR contrast without sacrificing N- $V^-$  fluorescence signal. This is unlike the use of a standard long-pass filter, which only partially filters out N- $V^0$  fluorescence while also sacrificing N- $V^-$  counts. First, we apply the charge-state determination method using resonant microwaves to establish the N- $V^-$  and N- $V^0$  spectral shapes for a given N- $V$  ensemble under the experimental conditions of interest, using the experimental setup shown in Fig. 1. This constitutes a one-off calibration measurement which, once performed for a given N- $V$  ensemble under a fixed set of experimental conditions, does not have to be repeated. The microwave frequency is then scanned over the resonance (as in a typical ODMR scan) and, at each scan point, spectra are acquired. The spectra are later fitted with the previously established N- $V^-$  and N- $V^0$  shapes and the N- $V^0$  contribution is discarded, allowing us to extract N- $V^-$ -only contrast as a function of the microwave frequency.

To enhance contrast usefully, the fitting procedure must yield an increased signal-to-noise ratio (SNR) in the measured ODMR contrast. If the fitting procedure that leads to an increase in contrast also proportionally increases the uncertainty on such contrast, then it delivers no gain in sensitivity. Here, we define our contrast-improvement figure of merit as a ratio of the SNRs:

$$\begin{aligned} \text{contrast improvement} &\equiv \frac{\text{SNR}_{\text{new}}}{\text{SNR}_{\text{undisc}}} \\ &= \frac{c_{\text{new}}/\delta c_{\text{new}}}{c_{\text{undisc}}/\delta c_{\text{undisc}}}, \end{aligned} \quad (11)$$

where  $\text{SNR}_{\text{undisc}}$  and  $\text{SNR}_{\text{new}}$  are, respectively, the SNRs in the measured ODMR contrast with the indiscriminated method and with our (fitting or tailored-weighting) method.  $\text{SNR}_{\text{new}} = c_{\text{new}}/\delta c_{\text{new}}$ , where  $c_{\text{new}}$  is the ODMR contrast obtained with our method and  $\delta c_{\text{new}}$  is an absolute error bar on this contrast. Similarly, for the indiscriminated method,  $\text{SNR}_{\text{undisc}} = c_{\text{undisc}}/\delta c_{\text{undisc}}$ .

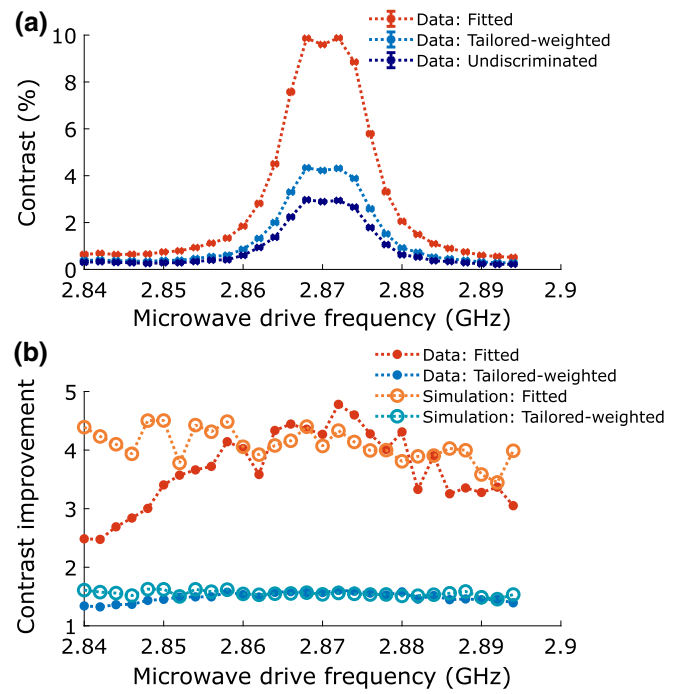


FIG. 8. (a) An ODMR scan taken on an N- $V$ -ensemble diamond sample using a spectrometer to collect fluorescence. The y axis plots the ODMR contrast, defined here as the difference in signal counts with microwaves off and on (the microwaves-on signal counts are subtracted from the microwaves-off signal counts) as a fraction of the microwaves-off signal counts. At each frequency, a sequence of 149 pairs of microwaves-on and microwaves-off spectra are taken. The contrast is calculated for each pair of spectra using all three methods: indiscriminated, tailored weighted, and fitted (the latter two methods are described in Secs. III B 2 and III B 1, respectively). The mean contrast obtained from the 149 shots is then plotted (undiscriminated in dark blue, tailored weighted in light blue, and fitted in orange), with error bars given by the standard deviation over all shots. The dotted lines connecting data points are guides to the eye. (b) The measured (filled markers) and simulated (hollow markers) contrast improvement, as defined by Eq. (11), for the fitting and tailored-weighting methods. For a description of the methods used to generate the simulated points, see the Appendix (Sec. A 3).

When we apply the fitting procedure to spectra taken from our diamond sample (at 7.3 mW of 532-nm laser power), we find a 4.8-fold contrast improvement compared to the indiscriminated contrast (Fig. 8), with the microwave drive resonant with the N- $V^-$  spin transition (i.e., at the point of maximum ODMR contrast). We calculate the improvement in SNR plotted in Fig. 8(b) by taking the ratio of the fractional error bars on the indiscriminated contrast to those on the fitted N- $V^-$  contrast.

To examine the limitations of the contrast-enhancement technique, we simulate the effect of applying it to synthetic data sets produced using the methods described in the Appendix (Sec. A 3). We examine the performance of the fitting technique in two scenarios: when the synthetic

data is photon-shot-noise limited and when the dominant source of noise is laser-intensity fluctuations between shots of the experiment. We find that in the shot-noise-limited case, the fitting technique produces no improvement in SNR. However, in the laser-intensity-noise-limited case, which most closely resembles our data, the simulation yields significant contrast improvements, particularly for samples with large  $N-V^0$  populations, as shown in Fig. 9. We also find that, for simulation parameters matching the experimental data shown in Fig. 8, the simulation yields a 4.3-fold contrast improvement (at the point of

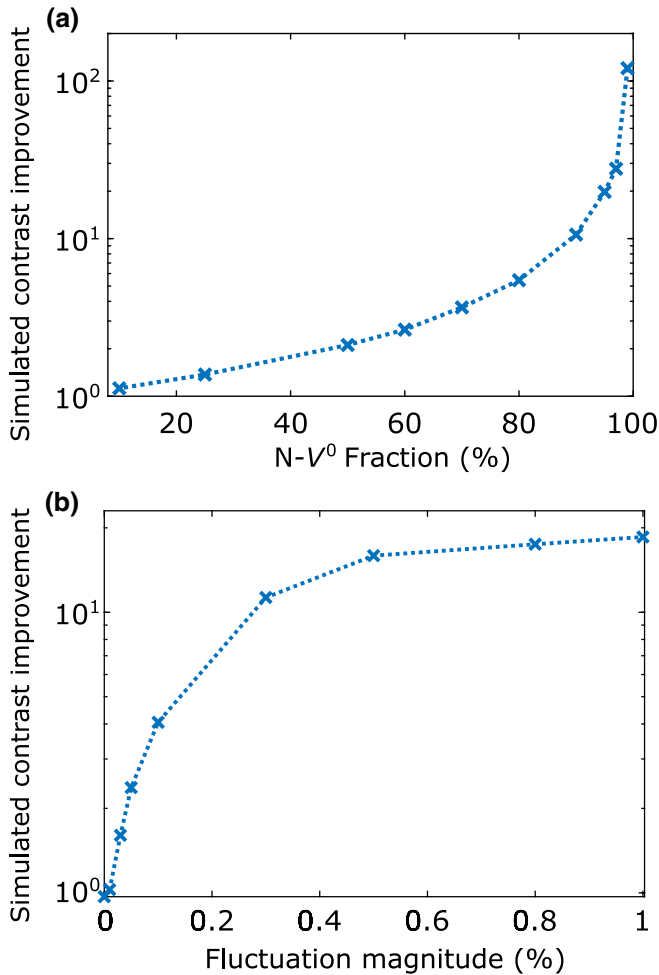


FIG. 9. The simulated ODMR contrast improvement for the *fitting method*. (a) The contrast improvement as a function of the  $N-V^0$  fraction (the fraction of the  $N-V$  ensemble’s fluorescence contributed by  $N-V^0$ ) at a fixed laser-intensity fluctuation magnitude of 1%. (b) The contrast improvement as a function of the laser-intensity fluctuation magnitude at an  $N-V^-$  fraction of 5%. Both simulations are run using the methods described in the Appendix (Sec. A 3) with a base microwaves-off spectrum with 19 315 132 counts and a pure- $N-V^-$  contrast of 10%. Note that the simulated contrast improvements plotted here are likely slightly underestimated because they do not account for the secondary effect of intensity-fluctuation-induced changes in the charge-state ratio (as discussed in Sec. III B 1, paragraph 7).

maximum ODMR contrast), in good agreement with our measurement.

An intuitive explanation for why there is no improvement in the shot-noise-limited case is the large overlap in wavelength between the  $N-V^0$  and  $N-V^-$  fluorescence spectra at room temperature. Photon shot noise, or Poisson noise, is a random process by which the number of photons in a given wavelength bin with mean photon number  $N$  fluctuates by an amount given by a Poisson distribution with standard deviation  $\sqrt{N}$ . The fitting procedure is subject to the Poisson noise from both  $N-V^0$  and  $N-V^-$  photons in each wavelength bin but can effectively weight down the photon noise in the wavelength bins that contain mostly  $N-V^0$  photons. The discarding of some  $N-V^0$  photon noise should yield an improvement in SNR, but if the  $N-V^0$  and  $N-V^-$  spectra largely overlap and the noise in each wavelength bin is not correlated to that in the neighboring bins, the fitting procedure cannot reliably distinguish  $N-V^0$  and  $N-V^-$  photons in the many wavelength bins that have similar numbers of  $N-V^-$  and  $N-V^0$  counts. Hence, at room temperature (when the  $N-V^-$  and  $N-V^0$  spectra overlap significantly), the fitting procedure does not yield an improvement in the SNR.

The situation is different if the dominant source of noise is technical, e.g., fluctuations in the intensity of the 532-nm laser or the microwave-field intensity. In this case, the main effect of the noise is, from shot to shot, to scale up or down the entire  $N-V^-$  (and  $N-V^0$ ) spectrum by a wavelength-independent scale factor, i.e., the fluctuation in all wavelength bins is, in this case, perfectly, or near-perfectly, correlated. If intensity noise causes the total number of counts to fluctuate on a time scale shorter than the delay between the acquisition of a microwaves-off and a microwaves-on spectrum, then fitting will offer an advantage in SNR. While the uncertainty on the undiscriminated contrast will be given by the total shot-to-shot fluctuation in fluorescence, the fitting procedure will be able to isolate the change in  $N-V^-$  fluorescence and discard the change in  $N-V^0$  counts, reducing the effect of intensity noise on the contrast measurement.

A second effect that allows our fitting method to offer further improvement in the SNR is the fact that any fluctuation in laser intensity will change the  $N-V^-$  to  $N-V^0$  ionization rate, leading to a change in the charge-state ratio of the ensemble from shot to shot. It is only when this effect is included in our simulations that we obtain good agreement with the data in Fig. 8. Without accounting for this effect, the simulation yields a more modest contrast improvement, of the order of  $3.5\times$ .

Provided that fluorescence readout with the spectrometer can be done at the same rate as readout with a photodiode (i.e., without introducing extra dead time into the experimental sequence), high-contrast ODMR performed using our fitting method will lead to increased sensitivity in laser or microwave intensity-noise-limited  $N-V$ -ensemble

magnetometers. In our current setup, our readout time is limited by the array shift time of our CCD to a few milliseconds. However, with the use of interline CCDs, which alternate sensor pixels with shift registers, readout of the full CCD array can be done in under  $2 \mu\text{s}$ , a delay that is negligible compared to the typical experimental sequence time.

## 2. Tailored-weighting method

The fitting technique provides contrast improvement only in technical-noise-limited applications. Here, we present a second contrast-enhancement method that can increase contrast even in shot-noise-limited applications, albeit with more modest improvement. The method involves weighting the acquired N- $V^-$  fluorescence spectrum by multiplying it (wavelength-bin-wise) by a tailored weighting function that weights each bin according to the expected fraction of N- $V^-$  photons it contains. Such a function would be defined as follows:

$$w_{\text{tailored}}(\lambda) = \frac{S_{\text{N-}V^-}(\lambda)}{S_{\text{N-}V^-}(\lambda) + S_{\text{N-}V^0}(\lambda)}, \quad (12)$$

where  $S_{\text{N-}V^-}(\lambda)$  and  $S_{\text{N-}V^0}(\lambda)$  are the N- $V^-$  and N- $V^0$  contributions to the microwaves-off spectrum, measured *a priori* with the spectrometer.

To enhance the ODMR contrast with this method, one would perform ODMR scans with a wavelength-discriminating detector and postprocess the data by multiplying both microwaves-on and microwaves-off spectra by  $w_{\text{tailored}}$  before evaluating contrast in the usual way (i.e., contrast = 1 – area under weighted microwaves-on spectrum/area under weighted microwaves-off spectrum). Note that when applied to the microwaves-on spectrum, this function will not perfectly weight each bin according to the expected N- $V^-$  fraction (as it does for the microwaves-off spectrum), since the ratio of N- $V^-$  to N- $V^0$  photons in each wavelength bin will be slightly altered from the microwaves-off ratio; however, the weighted microwaves-on spectrum will still preferentially enhance wavelength bins with larger N- $V^-$  contributions compared to the unweighted spectrum.

For a given sample and illumination conditions,  $w_{\text{tailored}}(\lambda)$  needs to be determined only once, *a priori*, by applying our microwave-modulated spectroscopy technique to decompose the microwaves-off spectrum into the N- $V^-$  and N- $V^0$  fluorescence contributions,  $S_{\text{N-}V^-}(\lambda)$  and  $S_{\text{N-}V^0}(\lambda)$ . After this calibration step, the method can be applied to any further measurements without the need to acquire additional spectra.

We apply the tailored-weighting method to real photoluminescence data collected from our diamond sample (which is not shot-noise limited) by postprocessing the microwaves-on and microwaves-off spectra as described above. We plot the results in Fig. 8, obtaining

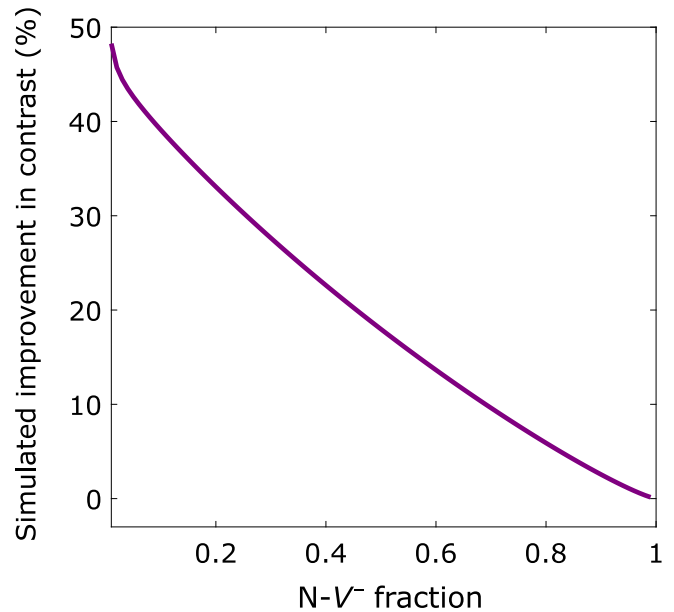


FIG. 10. The simulated SNR improvement in the ODMR contrast with the tailored-weighting method, plotted as a function of the N- $V^-$  fraction in the N- $V$  ensemble. A tailored weighting function,  $w_{\text{tailored}}(\lambda)$  [defined in Eq. (12)], is used to weight up the wavelength bins containing larger fractions of N- $V^-$  counts in both the microwaves-on and microwaves-off spectra. This method of postprocessing the N- $V$  fluorescence data offers contrast improvements even in shot-noise-limited applications.

an improvement in contrast for this particular ensemble of approximately 50% (i.e., enhancement by a factor of 1.5).

We also plot, in Fig. 10, the simulated improvement in the ODMR contrast produced by the tailored-weighting method when applied to shot-noise-limited synthetic data, as a function of the N- $V^-$  fluorescence fraction. The plot is produced by applying the weighting function  $w_{\text{tailored}}(\lambda)$  to shot-noise-limited synthetic data sets produced from the N- $V^-$  and N- $V^0$  basis spectra extracted from our N- $V$  diamond sample. Note that there is improvement at all N- $V^-$  fractions, with the greatest improvement in samples with a large N- $V^0$  population.

This simple method of postprocessing fluorescence data is hence a useful tool to improve contrast, even for shot-noise-limited applications.

## C. Spectral decomposition for other solid-state defects

As an example demonstration of how microwave-modulation methods may be used to isolate spectral features of other optically active solid-state defects, we modulate a 70-MHz rf drive applied to an ensemble of silicon vacancies in silicon carbide at room temperature, taking spectra with the rf drive on and off (Fig. 11). The 4H polytype of silicon carbide can host silicon vacancies (Si- $V$ s) at two inequivalent lattice sites. These are referred to as the V1 and V2 silicon vacancies. An ensemble of

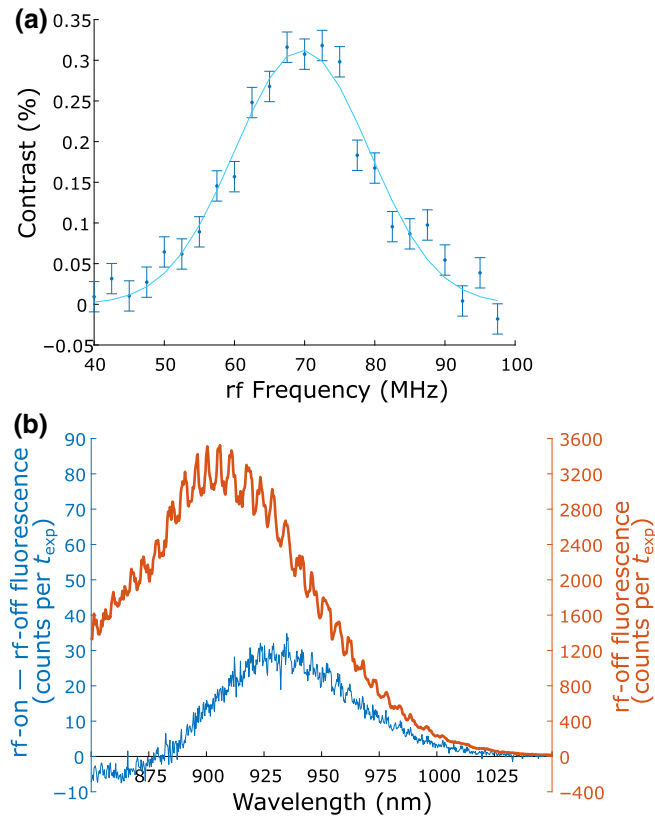


FIG. 11. The application of the microwave-assisted spectroscopic technique to a Si- $V$  ensemble in SiC. We use a confocal microscope to illuminate the sample with 760-nm light and to collect fluorescence. (a) The room-temperature ODMR spectrum of the Si- $V$  ensemble, identifying the V2 spin resonance at 70 MHz. The application of resonant rf transfers population to a brighter spin state and hence the contrast plotted on the y axis is defined here as  $(\text{rf-on counts} - \text{rf-off counts}) / \text{rf-off counts}$  (note that this is  $-1 \times$  the contrast definition that we use in this paper for ODMR in N- $V$  ensembles, where the application of microwaves transfers population to a dimmer spin state). These data are collected with an infrared-enhanced avalanche photodiode. (b) Orange: the rf-off spectrum of the Si- $V$  ensemble at room temperature. This spectrum is acquired with a spectrometer featuring an IR-enhanced CCD. Blue: the difference spectrum, extracted by taking the average difference between a series of PL spectra taken with the resonant 70 MHz rf drive on and a series of spectra taken with the rf drive off. Note that no flat-field corrections are applied to this spectrum.

these vacancies typically exhibits a very broad fluorescence spectrum (approximately 850 nm to 1050 nm) at room temperature, with no discernible ZPLs or distinguishing features between the V1 and V2 contributions to the fluorescence. Both exhibit spin-dependent fluorescence contrasts [33,34]; but the V1 has a spin-flip transition at 4 MHz, while the V2 transition occurs at 70 MHz. We can hence selectively modulate the V2 fluorescence with a 70-MHz rf drive. The resulting spectrum shown here [Fig. 11(b), blue data points] is simply the difference spectrum obtained by subtracting the rf-off spectrum from

the rf-on spectrum and has not been scaled or corrected for potential spin-dependent ionization effects. Figure 11(b) shows a difference spectrum that is significantly narrower than the total rf-off spectrum and is negative between 850 nm and 880 nm, suggesting that a spin-dependent transfer of population to other defect states (or charge states) may be occurring.

#### IV. DISCUSSION

The microwave-assisted method of charge-state-ratio determination presented here benefits from being tailored to the sample and experimental conditions under investigation. The extraction of the N- $V^-$  and N- $V^0$  spectra *in situ* ensures that our measurement of the charge-state ratio accounts for any changes in the shape of the N- $V^-$  and N- $V^0$  fluorescence spectra due to sample-specific material properties (such as the local strain) or experimental parameters (such as the temperature and the excitation wavelength). We note that the use of charge-state-determination methods that do not account for changes in the N- $V^-$  and N- $V^0$  spectral shape—such as methods that decompose a sample spectrum by doing least-squares fitting with literature-reported N- $V^-$  and N- $V^0$  spectra extracted from a different sample, or methods that compare the area under the N- $V^-$  and N- $V^0$  ZPLs to extract charge-state ratio—are likely to yield inaccurate results. The former approach assumes no change in the N- $V^-$  and N- $V^0$  fluorescence spectra across different samples and experimental setups, and the latter relies on a fixed (or, at least, known) proportion of the total fluorescence from each charge state being emitted in the ZPL. However, both the spectral shape and the proportion of fluorescence in the ZPL may vary from sample to sample and even from site to site in a given diamond. It is hence difficult to compare charge-state measurements by these methods across different samples. This in turn limits the usefulness of such methods in identifying which material and experimental parameters can be tuned to produce the N- $V^-$ -rich diamonds needed for high-sensitivity magnetometry.

The method presented here produces charge-ratio measurements that can be compared across different diamond samples and experimental conditions. In particular, it allows the investigation of the charge-state ratio under any illumination sequence that optically pumps the N- $V^-$  state to  $m_s=0$  and produces a fluorescence contrast between the  $m_s=0$  and  $m_s=\pm 1$  states of N- $V^-$ . This permits the investigation of the charge-state ratio as a function of the illumination duration, intensity, and wavelength.

Further, our approach allows us to accurately describe the N- $V^-$   $^3E$  to  $^3A_2$  (and N- $V^0$   $^2A_2$  to  $^2E$ ) phonon sidebands, without contamination from the phonon sidebands of the other charge state. This can yield more accurate one-phonon spectra, from which we can obtain a better understanding of the N- $V$  vibrational modes and electronic wave functions [35].

The analysis presented here may also be adapted to work with other methods of selectively modulating  $N-V^-$  fluorescence, such as magnetic-field-induced spin-polarization quenching [14,25].

Using our technique, we uncover evidence for a spin-dependent ionization pathway from the singlet states of  $N-V^-$ , which manifests as a negative  $N-V^0$  fluorescence contrast (implying an increase of the  $N-V^0$  population when the microwaves are on) at a wide range of laser powers. An understanding of the regimes under which this mechanism dominates ionization dynamics in  $N-V$  ensembles is crucial for optimizing the fabrication of diamonds for high-sensitivity magnetometry and for scaling up the implementation of readout techniques involving spin-to-charge conversion.

We also show that our method can be used to enhance the ODMR contrast by discarding or preferentially weighting down the  $N-V^0$  fluorescence contribution. The high-contrast ODMR techniques we present here may lead to significant sensitivity improvements in  $N-V$  magnetometers, especially when the  $N-V^0$  population is significant. This is particularly relevant to near-surface  $N-V$  ensembles, where the energetically preferred charge state is  $N-V^0$ .  $N-V$  magnetometers are typically used to measure fields from samples placed on the diamond surface, so near-surface  $N-V$ s are exposed to the largest magnetic field amplitudes and can offer the highest-resolution measurements. However, a poor ODMR contrast due to a large  $N-V^0$  population may limit their use in applications that require high sensitivity. Our *fitting method* may significantly improve the sensitivity of magnetometry with near-surface  $N-V$  ensembles, leading to significant advances in applications such as live imaging of biological processes [21] and picoliter nuclear magnetic resonance [36].

Finally, we show that our method may be applied to isolate spectral features of other fluorescent solid-state defects (such as V1 and V2 silicon vacancies in silicon carbide [37]), facilitating the study of their optical and spin properties.

## ACKNOWLEDGMENTS

We thank Y. Zhu for fabricating the microwave stripline board used to deliver microwaves to the  $N-V$  ensemble in this work and J. Dietz for assisting with optical characterization. This work was partially supported by the National Science Foundation (NSF) Science and Technology Center (STC) for Integrated Quantum Materials, NSF Grant No. DMR-1231319, the Air Force Office of Scientific Research Award No. FA9550-17-1-0371, the Army Research Office Grant No. W911NF-15-1-0548, and the NSF EARly-concept Grants for Exploratory Research (EAGER) Grant No. ECCS 1748106. J.M.S. was supported by a Fannie and John Hertz Foundation Graduate Fellowship and a NSF Graduate Research Fellowship under Grant No. 1122374.

The authors D.P.L.A.C. and P.K. developed the microwave-modulation technique for measuring the fluorescence intensity ratio of  $N-V^-$ -to- $N-V^0$ . D.P.L.A.C. identified, corrected for, and developed a rate-equation model for spin-dependent ionization effects, developed and modeled the contrast-enhancement ODMR techniques, took and analyzed the data, and wrote the PYTHON software for data acquisition. D.P.L.A.C. and A.S.G. set up the optical path for the diamond experiments. A.S.G. and X.Z. set up the optical path for applying the method to SiC and assisted in taking data on the SiC sample. M.J.T. tested the charge-ratio determination technique on a second optical setup. J.M.S., E.B., and C.H. posed the problem of accurately determining the charge state in  $N-V$  ensembles, reviewed the literature, and participated in discussions. E.L.H. and R.L.W. supervised the project. All authors discussed the results and proofread the manuscript.

## APPENDIX

### 1. Experimental setup and diamond properties

The  $N-V$  experiments described here are performed on a home-built confocal microscope featuring a 100 $\times$  objective lens of numerical aperture 0.90.

The excitation light is provided by a 532-nm diode-pumped solid-state laser (Coherent Verdi V10). The spot size at the sample is measured to be approximately 1.2  $\mu\text{m}$  in diameter. The laser intensity is stabilized by a commercial noise-eater circuit (Thorlabs NEL01).

$N-V$  fluorescence (separated from the excitation light by a dichroic filter) is passed through a grating spectrometer (Acton Research Corporation SpectraPro-500) and collected on a liquid-nitrogen-cooled CCD (Roper Scientific LN/CCD-1340/400-EB/1). We note that no flat-field calibration is applied to the collected spectra.

The microwave drive is provided by a signal generator (SRS 384) and applied to the diamond through an omega-loop stripline fabricated by deposition of gold on silicon carbide. A TTL-triggered microwave switch (Minicircuits ZASWA-2-50DR+) is used to turn the microwave drive on and off for the acquisition of microwaves-on and microwaves-off spectra in quick succession.

A multichannel TTL pulse generator (Spincore PulseBlaster), controlled by an expanded version of the qdSpecPro PYTHON package [13], is used to synchronously trigger CCD exposures and the microwave switch. The spectra obtained here are averaged over a series of up to approximately 20 000 CCD frames, with subsequent acquisitions taken with microwaves on and microwaves off. The CCD is exposed for an exposure time of  $t_{\text{exp}} \geq 30$  ms to acquire each frame.

Data are collected with no applied magnetic field (except for the Earth's field, which is not canceled). To determine the resonance frequency at which the microwave drive should be applied, an ODMR spectrum

is acquired before the series of PL spectra are taken. The microwave-drive frequency is chosen to match an ODMR resonance.

The diamond used for the experiments presented here is provided by Element Six. It contains a 10- $\mu\text{m}$ -thick N-V layer (10 ppm  $^{14}\text{N}$ , >99.95%  $^{12}\text{C}$ ) grown by chemical vapor deposition (CVD) on an electronic-grade single-crystal substrate. This sample is irradiated with a dosage of  $6 \times 10^{18}$  electrons per  $\text{cm}^2$  and annealed for 12 h at 800 °C and for 12 h at 1000 °C.

## 2. Rate-equation model of spin-dependent ionization effects

To produce the model plotted in Fig. 6, we use the rates listed in Table I. All rates are extracted from the literature, with the exception of the N- $V^-$  excitation rate,  $a_e P$  (i.e., the rate of transition from levels 1 and 2 to levels 3 and 4), and the rate of postulated ionization from the N- $V^-$  shelf,  $a_s P$ , which are both floated in a fit to the data. The fitted value for the N- $V^-$  excitation-rate coefficient,  $a_e = 5.9 \times 10^{-5}$ , is close to our estimate of  $2.3 \times 10^{-5}$ , obtained from our spot-size radius of approximately 0.6  $\mu\text{m}$  and the literature value of the N- $V^-$  absorption cross section of  $9.5 \times 10^{-17} \text{cm}^2$  [38].

We model laser-driven transitions between pairs of levels as having rates  $a_n P$ , where  $P$  is the 532-nm laser power and  $a_n$  is a scalar coefficient. We use the ratios of the N- $V^-$  ionization rate, the N- $V^0$  excitation rate, and the N- $V^0$  recombination rate to the N- $V^-$  excitation rate reported in Ref. [39] to determine, for a given N- $V^-$  excitation-rate coefficient,  $a_e$ , our model coefficients  $a_i$ ,  $a_0$ , and  $a_r$ . These coefficients describe, respectively, the N- $V^-$  ionization rate,  $a_i P$  (from levels 3 or 4 to level 6), the N- $V^0$  excitation rate,  $a_0 P$  (from level 6 to level 7), and the N- $V^0$  recombination rate,  $a_r P$  (from level 7 to levels 1 and 2), in our model.

Our model takes transitions between the N- $V^-$  triplet ground and excited states to be perfectly spin conserving, an assumption that is good to 4% [12]. With this assumption, we extract rates of spontaneous decay,  $k_{31}$ ,  $k_{42}$ ,  $k_{35}$ ,  $k_{45}$ ,  $k_{51}$ , and  $k_{52}$ , from Ref. [12]. The N- $V^-$  ground-state spin-flip rate ( $m_{12} = m_{21}$ ) is determined from the  $\pi$ -pulse time from measured Rabi flops and we ignore spontaneous decay from level 2 to level 1, as it happens on the time scale of the  $T_1$  time, which is an order of magnitude slower than the slowest transition rate in our model (for laser powers above 10  $\mu\text{W}$ ).

Finally, we include the phenomena of ionization and recombination in the dark reported in the literature [40,41] by linking the ground-state levels of N- $V^-$  and N- $V^0$  with two transition rates,  $d_i$  and  $d_r$ , representing dark ionization (from levels 1 and 2 to level 6) and recombination (from level 6 to levels 1 and 2), respectively. We set  $d_i = 100 \mu\text{s}^{-1}$ , since the ionization rates reported in the

literature from shallow N- $V$ s vary from 100  $\mu\text{s}$  to seconds [41]. From Eq. (9), one can see that setting  $P = 0$  yields  $d_r/d_i = [p_1(0) + p_2(0)]/p_6(0)$ , where the right-hand side of this equation corresponds to the ratio of the N- $V^-$  to the N- $V^0$  population in the dark. Hence, we set the ratio  $d_r/d_i$  according to our measured charge-state ratio at the lowest laser power with which we measure our ensemble (in our case, 10  $\mu\text{W}$ ).

## 3. Simulations of SNR enhancement in ODMR

To simulate the contrast enhancement achievable with the fitting technique described in Sec. III B 1 of the main text, we produce two simulated, or synthetic, data sets—one shot-noise-limited data set and one laser-intensity-noise-limited data set. In this section, we describe how the two data sets are generated.

To create the two synthetic data sets, we start by scaling up a pure N- $V^-$  spectrum and a pure N- $V^0$  spectrum (both determined from real data) so that the total counts correspond to the typical number counts we collect from our sample (at a given laser power and spectrometer-CCD exposure time) and the ratio of counts in the N- $V^0$  and N- $V^-$  spectra matches the charge-state ratio we want to simulate. These N- $V^-$  and N- $V^0$  component spectra are then summed to give a total microwaves-off spectrum. To produce a microwaves-on spectrum, we reduce the counts in the N- $V^-$  component by some scale factor, which we choose to match the pure-N- $V^-$  contrast we want to simulate (i.e., the fluorescence contrast that would be exhibited by N- $V^-$ ; for our experimental conditions and sample, we measure this to be 10%). We henceforth refer to this pair of microwaves-on and off spectra as the base spectra.

To produce the shot-noise-limited synthetic data set, we simulate photon statistics: 149–500 versions, or “shots,” of the base microwaves-off and microwaves-on spectra are generated, each with random Poisson fluctuations applied to the number of photon counts per wavelength bin. Each simulated shot of the spectrum is created by replacing the number of counts  $N_i$  in each wavelength bin  $\lambda_i$  with a random number of counts sampled from a Poisson distribution with mean  $N_i$ .

To simulate the laser-intensity-noise-limited data set, we generate the sequence of 149–500 shots of alternating microwaves-on and microwaves-off spectra by repeating the procedure we use to create the shot-noise-limited data set but now introducing a Gaussian-distributed fluctuation in the total number of counts in each shot ( $N_{\text{off}}$ ). The fluctuation in counts is implemented by adding, to the base spectra’s microwaves-off counts, a random number sampled from a Gaussian distribution of mean zero and standard deviation  $\sigma_c$ , where  $\sigma_c$  is chosen to match observed fluctuations in microwaves-off counts in real data. Poisson fluctuations are then also introduced to each wavelength bin (as with the shot-noise-limited data set before). In the

data set shown in Fig. 8,  $N_{\text{off}}$  fluctuates, on average, by 0.33%.

To simulate the improvement in contrast attainable with our fitting method, we fit each pair of microwaves-on and microwaves-off “shots” in the simulated sequence with a pure  $N-V^-$  and a pure  $N-V^0$  spectrum to extract the fitted  $N-V^-$  contrast (see main text, Sec. III B 1). We then calculate the mean and the standard deviation of the fitted  $N-V^-$  contrast ( $\overline{C_{\text{fitted}}}$  and  $\sigma_{\text{fitted}}$  respectively) and the undiscriminated contrast ( $\overline{C_{\text{undisc}}}$  and  $\sigma_{\text{undisc}}$  respectively) across all microwaves-off–microwaves-on “shots.” Finally, we take the ratio of the fractional error on the undiscriminated contrast to that on the fitted  $N-V^-$  contrast to determine improvement, as follows:

$$\text{contrast improvement} = \frac{\sigma_{\text{undisc}}/\overline{C_{\text{undisc}}}}{\sigma_{\text{fitted}}/\overline{C_{\text{fitted}}}}. \quad (\text{A1})$$

With this definition [which is equivalent to that in Eq. (11) in the main text], we find no contrast improvement from our fitting method in the shot-noise-limited case but significant improvements in the laser-intensity-noise-limited case, particularly for large  $N-V^0$  populations (Fig. 9).

To simulate the experiment that generates the data in Fig. 8, we set the simulation parameters to match the properties of the  $N-V$  sample that we measure and the laser-intensity noise that we record: the base-spectra microwaves-off counts are set to  $N_{\text{off}} = 19\,903\,285$ , the standard-deviation magnitude of the shot-to-shot fluctuations in microwaves-off counts to  $\sigma_c = 0.33\%$ , and the sample’s pure- $N-V^-$  contrast to 9.7%. We also include a secondary effect of the laser-intensity noise: a shot-to-shot fluctuation in the charge-state ratio due to the change in the laser intensity (which leads to a change in the  $N-V^-$ -to- $N-V^0$  ionization rate). By plotting the measured shot-to-shot change in the charge-state ratio versus the shot-to-shot change in the total microwaves-off counts and fitting a straight line through the data, we infer that the  $N-V^-$  fraction of the fluorescence fluctuates, on average, by  $-0.21\times$  the fluctuation in laser intensity from shot-to-shot. For simplicity, we simulate this fluctuation in the charge-state ratio as being perfectly correlated to the fluctuation in the laser intensity (i.e., the fluctuation in the  $N-V^-$  fraction from shot to shot equals  $-0.21$  times the fluctuation in the laser intensity) but the correlation is not perfect in the data (the correlation coefficient is  $-0.55$ ). The inclusion of this secondary effect in our simulations gives a simulated 4.3-fold contrast improvement for the fitting method, which is in good agreement with the measured value. If this effect is not included, the simulation yields a more modest improvement of  $3.5\times$ .

In Fig. 8, we also plot the simulated (and measured) contrast improvement for the tailored-weighting method. We simulate the improvement by applying the tailored-weighting method to the synthetic data set

described in the previous paragraph. As described in Sec. III B 2 of the main text, this involves multiplying both the simulated microwaves-on and the microwaves-off spectra by the tailored weighting function  $w_{\text{tailored}}$  and then calculating the contrast in the usual way.

Finally, to produce Fig. 10 in the main text, we simulate the contrast enhancement achievable with the tailored-weighting technique in the shot-noise-limited case as a function of the  $N-V^-$  fraction. The improvement can be calculated analytically since, if the dominant source of noise is photon shot noise, the error bars on the ODMR contrast can be calculated by means of Poisson statistics.

- 
- [1] R. Schirhagl, K. Chang, M. Loretz, and C. L. Degen, Nitrogen-vacancy centers in diamond: Nanoscale sensors for physics and biology, *Ann. Rev. Phys. Chem.* **65**, 83 (2014).
  - [2] K. Jensen, P. Kehayias, and D. Budker, in *High Sensitivity Magnetometers, Smart Sensors, Measurement and Instrumentation*, edited by A. Grosz, M. J. Haji-Sheikh, and S. C. Mukhopadhyay (Springer International Publishing, Switzerland, 2017), Chap. 18, p. 553.
  - [3] F. Casola, T. van der Sar, and A. Yacoby, Probing condensed matter physics with magnetometry based on nitrogen-vacancy centres in diamond, *Nat Rev Mater* **3**, 17088 (2018).
  - [4] D. Le Sage, K. Arai, D. Glenn, S. DeVience, L. Pham, L. Rahn-Lee, M. Lukin, A. Yacoby, A. Komeili, and R. Walsworth, Optical magnetic imaging of living cells, *Nature* **496**, 486 (2013).
  - [5] D. R. Glenn, K. Lee, H. Park, R. Weissleder, A. Yacoby, M. D. Lukin, H. Lee, R. L. Walsworth, and C. B. Connolly, Single-cell magnetic imaging using a quantum diamond microscope, *Nat. Methods* **12**, 736 (2015).
  - [6] H. C. Davis, P. Ramesh, A. Bhatnagar, A. Lee-Gosselin, J. F. Barry, D. R. Glenn, R. L. Walsworth, and M. G. Shapiro, Mapping the microscale origins of magnetic resonance image contrast with subcellular diamond magnetometry, *Nat. Commun.* **9**, 131 (2018).
  - [7] J. F. Barry, M. J. Turner, J. M. Schloss, D. R. Glenn, Y. Song, M. D. Lukin, H. Park, and R. L. Walsworth, Optical magnetic detection of single-neuron action potentials using quantum defects in diamond, *Proc Natl Acad Sci* **113**, 14133 (2016).
  - [8] R. R. Fu, B. P. Weiss, E. A. Lima, P. Kehayias, J. F. Araujo, D. R. Glenn, J. Gelb, J. F. Einsle, A. M. Bauer, R. J. Harrison, G. A. Ali, and R. L. Walsworth, Evaluating the paleomagnetic potential of single zircon crystals using the Bishop Tuff, *Earth Planet. Sci. Lett.* **458**, 1 (2017).
  - [9] B. P. Weiss, R. R. Fu, J. F. Einsle, D. R. Glenn, P. Kehayias, E. A. Bell, J. Gelb, J. F. Araujo, E. A. Lima, C. S. Borlina *et al.*, Secondary magnetic inclusions in detrital zircons from the Jack Hills, Western Australia, and implications for the origin of the geodynamo, *Geology* **46**, 427 (2018).
  - [10] T. Wolf, P. Neumann, K. Nakamura, H. Sumiya, T. Ohshima, J. Isoya, and J. Wrachtrup, Subpicotesla Diamond Magnetometry, *Phys. Rev. X* **5**, 041001 (2015).

- [11] J. F. Barry, J. M. Schloss, E. Bauch, M. J. Turner, C. A. Hart, L. M. Pham, and R. L. Walsworth, Sensitivity optimization for NV-diamond magnetometry, *Rev. Mod. Phys.* **92**, 015004 (2020).
- [12] L. Robledo, H. Bernien, T. van der Sar, and R. Hanson, Spin dynamics in the optical cycle of single nitrogen-vacancy centres in diamond, *New J. Phys.* **13**, 025013 (2011).
- [13] D. P. L. A. Craik, qdSpectro, Zenodo 10.5281/zenodo.3378208 (2019).
- [14] N. B. Manson, M. Hedges, M. S. J. Barson, R. Ahlefeldt, M. W. Doherty, H. Abe, T. Ohshima, and M. J. Sellars, NV<sup>-</sup> – N<sup>+</sup> pair centre in 1b diamond, *New J. Phys.* **20**, 113037 (2018).
- [15] N. Aslam, G. Waldherr, P. Neumann, F. Jelezko, and J. Wrachtrup, Photo-induced ionization dynamics of the nitrogen vacancy defect in diamond investigated by single-shot charge state detection, *New J. Phys.* **15**, 013064 (2013).
- [16] X.-D. Chen, C.-L. Zou, F.-W. Sun, and G.-C. Guo, Optical manipulation of the charge state of nitrogen-vacancy center in diamond, *Appl. Phys. Lett.* **103**, 013112 (2013).
- [17] P. Ji, R. Balili, J. Beaumariage, S. Mukherjee, D. Snoke, and M. V. G. Dutt, Multiple-photon excitation of nitrogen vacancy centers in diamond, *Phys. Rev. B* **97**, 134112 (2018).
- [18] N. Manson and J. Harrison, Photo-ionization of the nitrogen-vacancy center in diamond, *Diam. Relat. Mater.* **14**, 1705 (2005).
- [19] D. B. Bucher, D. P. L. Aude Craik, M. P. Backlund, M. J. Turner, O. Ben Dor, D. R. Glenn, and R. L. Walsworth, Quantum diamond spectrometer for nanoscale NMR and ESR spectroscopy, *Nat. Protoc.* **14**, 2707 (2019).
- [20] Y. Dovzhenko, F. Casola, S. Schlotter, T. Zhou, F. Büttner, R. Walsworth, G. Beach, and A. Yacoby, Magneto-static twists in room-temperature skyrmions explored by nitrogen-vacancy center spin texture reconstruction, *Nat. Commun.* **9**, 2712 (2018).
- [21] J. F. Barry, M. J. Turner, J. M. Schloss, D. R. Glenn, Y. Song, M. D. Lukin, H. Park, and R. L. Walsworth, Optical magnetic detection of single-neuron action potentials using quantum defects in diamond, *Proc. Natl. Acad. Sci.* **113**, 14133 (2016).
- [22] L. M. Pham, D. L. Sage, P. L. Stanwix, T. K. Yeung, D. Glenn, A. Trifonov, P. Cappellaro, P. R. Hemmer, M. D. Lukin, H. Park, A. Yacoby, and R. L. Walsworth, Magnetic field imaging with nitrogen-vacancy ensembles, *New J. Phys.* **13**, 045021 (2011).
- [23] X.-D. Chen, C.-H. Dong, F.-W. Sun, C.-L. Zou, J.-M. Cui, Z.-F. Han, and G.-C. Guo, Temperature dependent energy level shifts of nitrogen-vacancy centers in diamond, *Appl. Phys. Lett.* **99**, 161903 (2011).
- [24] T. L. McCormick, W. E. Jackson, and R. J. Nemanich, The characterization of strain, impurity content, and crush strength of synthetic diamond crystals, *J. Mater. Res.* **12**, 253 (1997).
- [25] R. Giri, C. Dorigoni, S. Tambalo, F. Gorrini, and A. Bifone, Selective measurement of charge dynamics in an ensemble of nitrogen-vacancy centers in nanodiamond and bulk diamond, *Phys. Rev. B* **99**, 155426 (2019).
- [26] J. Stortebom, P. Dolan, S. Castelletto, X. Li, and M. Gu, Lifetime investigation of single nitrogen vacancy centres in nanodiamonds, *Opt. Express* **23**, 11327 (2015).
- [27] T. Mittiga, S. Hsieh, C. Zu, B. Kobrin, F. Machado, P. Bhattacharyya, N. Z. Rui, A. Jarmola, S. Choi, D. Budker, and N. Y. Yao, Imaging the Local Charge Environment of Nitrogen-Vacancy Centers in Diamond, *Phys. Rev. Lett.* **121**, 246402 (2018).
- [28] D. Hopper, H. Shulevitz, and L. Bassett, Spin readout techniques of the nitrogen-vacancy center in diamond, *Micromachines* **9**, 437 (2018).
- [29] E. Bourgeois, A. Jarmola, P. Siyushev, M. Gulka, J. Hruby, F. Jelezko, D. Budker, and M. Nesladek, Photoelectric detection of electron spin resonance of nitrogen-vacancy centres in diamond, *Nat. Commun.* **6**, 8577 (2015).
- [30] B. J. Shields, Q. P. Unterreithmeier, N. P. de Leon, H. Park, and M. D. Lukin, Efficient Readout of a Single Spin State in Diamond via Spin-to-Charge Conversion, *Phys. Rev. Lett.* **114**, 136402 (2015).
- [31] R. P. Roberts, M. L. Juan, and G. Molina-Terriza, Spin-dependent charge state interconversion of nitrogen vacancy centers in nanodiamonds, *Phys. Rev. B* **99**, 174307 (2019).
- [32] H. Jayakumar, S. Dhomkar, J. Henshaw, and C. A. Meriles, Spin readout via spin-to-charge conversion in bulk diamond nitrogen-vacancy ensembles, *Appl. Phys. Lett.* **113**, 122404 (2018).
- [33] M. Widmann, S.-Y. Lee, T. Rendler, N. T. Son, H. Fedder, S. Paik, L.-P. Yang, N. Zhao, S. Yang, I. Booker *et al.*, Coherent control of single spins in silicon carbide at room temperature, *Nat. Mater.* **14**, 164 (2015).
- [34] R. Nagy, M. Widmann, M. Niethammer, D. B. R. Dasari, I. Gerhardt, O. O. Soykal, M. Radulaski, T. Ohshima, J. Vučković, N. T. Son, I. G. Ivanov, S. E. Economou, C. Bonato, S.-Y. Lee, and J. Wrachtrup, Quantum Properties of Dichroic Silicon Vacancies in Silicon Carbide, *Phys. Rev. Appl.* **9**, 034022 (2018).
- [35] P. Kehayias, M. W. Doherty, D. English, R. Fischer, A. Jarmola, K. Jensen, N. Leefer, P. Hemmer, N. B. Manson, and D. Budker, Infrared absorption band and vibronic structure of the nitrogen-vacancy center in diamond, *Phys. Rev. B* **88**, 165202 (2013).
- [36] D. R. Glenn, D. B. Bucher, J. Lee, M. D. Lukin, H. Park, and R. L. Walsworth, High-resolution magnetic resonance spectroscopy using a solid-state spin sensor, *Nature* **555**, 351 (2018).
- [37] E. Janzén, A. Gali, P. Carlsson, A. Gällström, B. Magnusson, and N. Son, The silicon vacancy in SiC, *Phys. B: Condensed Matter* **404**, 4354 (2009).
- [38] R. Chapman and T. Plakhotnik, Anomalous saturation effects due to optical spin depolarization in nitrogen-vacancy centers in diamond nanocrystals, *Phys. Rev. B* **86**, 045204 (2012).
- [39] L. Hacquebard and L. Childress, Charge-state dynamics during excitation and depletion of the nitrogen-vacancy center in diamond, *Phys. Rev. A* **97**, 063408 (2018).
- [40] R. Giri, F. Gorrini, C. Dorigoni, C. E. Avalos, M. Cazzanelli, S. Tambalo, and A. Bifone, Coupled charge and spin dynamics in high-density ensembles of nitrogen-vacancy centers in diamond, *Phys. Rev. B* **98**, 045401 (2018).
- [41] D. Bluvstein, Z. Zhang, and A. C. B. Jayich, Identifying and Mitigating Charge Instabilities in Shallow Diamond Nitrogen-Vacancy Centers, *Phys. Rev. Lett.* **122**, 076101 (2019).